Biophysical Journal
Article

Biophysical Society

Interplay between Brownian motion and cross-linking controls bundling dynamics in actin networks

Ondrej Maxian,[1,*] Aleksandar Donev,[1] and Alex Mogilner[1,2]
[1]Courant Institute, New York University, New York, New York and [2]Department of Biology, New York University, New York, New York

ABSTRACT Morphology changes in cross-linked actin networks are important in cell motility, division, and cargo transport. Here, we study the transition from a weakly cross-linked network of actin filaments to a heavily cross-linked network of actin bundles through microscopic Brownian dynamics simulations. We show that this transition occurs in two stages: first, a composite bundle network of small and highly aligned bundles evolves from cross-linking of individual filaments and, second, small bundles coalesce into the clustered bundle state. We demonstrate that Brownian motion speeds up the first stage of this process at a faster rate than the second. We quantify the time to reach the composite bundle state and show that it strongly increases as the mesh size increases only when the concentration of cross-links is small and that it remains roughly constant if we decrease the relative ratio of cross-linkers as we increase the actin concentration. Finally, we examine the dependence of the bundling timescale on filament length, finding that shorter filaments bundle faster because they diffuse faster.

SIGNIFICANCE Eukaryotic cells contain an actin cytoskeleton that gives the cell its structure and controls its mechanical properties. In this work, we consider two main components of the cytoskeleton, actin fibers and transient cross-linkers, and show how the action of the cross-linkers can transition the filament structure from a homogeneous meshwork of filaments, which flows easily, to a network of tightly cross-linked bundles, which has a high resistance to deformation. We discuss how Brownian motion and cross-linking combine to yield a timescale for the bundling process and quantify how this timescale depends on the filament length and concentration and the amount of cross-linking protein in the system.

INTRODUCTION

The structure and mechanical properties of eukaryotic cells are largely controlled by the actin cytoskeleton, which contains a network of actin filaments interconnected by protein cross-linkers (CLs) (1,2). Changes in cell mechanical properties, from more viscous to more elastic, relate to corresponding cytoskeletal morphology changes, from a weakly cross-linked network of actin filaments to a network of clustered bundles (3,4). The formation of a clustered bundle state has previously been observed in actin suspensions with CLs, such as filamin (5,6), scruin (7), and α-actinin (8,9). In all of these systems, increasing the concentration of the cross-linking protein progressively transitions the steady state from a homogeneous meshwork, where filaments are distributed isotropically, through a composite bundle state, where bundles are composed of only a few filaments, to the clustered bundle state, where bundles can be separated by distances as large as 100 μm (5,8).

Usually, the bundled network steady state is the result of a balance between cross-linking and other mechanisms that break up bundles. Indeed, in our previous work (3), we introduced actin filament turnover (to model [de]polymerization) and found that the steady-state network morphology is the result of a competition between actin bundling and actin turnover. In particular, we observed either a homogeneous filament meshwork or network of bundles embedded in the filament meshwork, depending on the relationship between the turnover time and the timescale of filament bundling. In most of this paper, we will disable filament turnover and study how the timescale of bundling, which we define approximately as the time to reach the composite bundle state, is affected by the underlying microscopic parameters and the Brownian motion of the filaments. Quantifying this timescale is important because its competition

Submitted September 17, 2021, and accepted for publication February 16, 2022.

*Correspondence: om759@nyu.edu

Editor: Dimitrios Vavylonis.
https://doi.org/10.1016/j.bpj.2022.02.030

with filament turnover rate determines the steady-state network structure, as we will demonstrate.

Although it was observed over 30 years ago (6) that Brownian motion drives bundle formation, its precise mechanism for doing so remains unclear. For instance, Hou et al. (6) speculated that rotational diffusion aids in bundling, as filaments that are linked at one location rotate until other locations can be linked together, resulting in a bundle. More recently, it was shown that bundling is most efficient in a fluid-like environment, where actin filaments can diffuse more readily (10,11). At minimum, these studies imply that bundling is more difficult without Brownian motion, but could actin filaments still arrange into bundles without it?

The importance of Brownian motion in bundling can be seen in experiments where filament length varies or when polymerization and bundling are initiated simultaneously. In this case, shorter filaments form a more stable clustered bundle state (12,11), with the shortest filaments organizing into spindle-type structures (13,14). In systems where polymerization and bundling happen simultaneously, it has been shown that the formation of the clustered bundle state can be prevented via an increase in the actin polymerization rate (10). Mean field theory and simulations show that the slow down in bundling at high polymerization rates could be driven by a combination of steric interactions and the Brownian motion of the fibers being constrained by CLs (11). It remains unclear, however, to what extent the attenuation of bundling is driven by sterics versus cross-linking and even whether a composite bundle state can form if the length of the filaments is larger than the initial mesh size.

An underlying assumption in conceptual explanations of bundling is that sufficient CL is available to cross-link filaments once they move closer together. The literature is conflicted, however, on exactly how much CL is sufficient. For instance, in the same experimental system of filamin and actin, some authors report a constant ratio of CL to actin necessary for bundling (6,9), although others report that the relative amount of CL necessary for bundling decreases as actin concentration increases (5). There is also a nontrivial effect of temperature on the amount of CL required for bundling; with higher CL-to-actin ratios, bundling can occur at lower temperatures (15). Experimental investigation of the precise amount of CL necessary for the clustered bundle state to form is difficult since the observation of bundles is a qualitative phenomenon with a subjective definition and therefore varies based on the tools used. Simulations can provide a more definitive analysis of how bundling depends on CL concentration.

Two simulation approaches have been used to theorize about the bundling of actin filaments. One of them was to use equilibrium thermodynamics to find conditions at which the free energy, consisting of translational and rotational entropy of rod-like filaments and enthalpy and entropy of the CL distribution, is lower in the bundled state than in the unbundled mesh (16,17). The important results of these theories were that a critical CL concentration is needed for the bundling phase transition and that ultimately one giant bundle has to form, but transiently, the filaments could be kinetically trapped in multiple bundles (16,18). However, actin bundling is not taking place in thermodynamic equilibrium, and several modeling studies harnessed the Brownian dynamics approach. One of the earliest (19) of these studied the roles of translational and rotational diffusion in bundling of uniformly laterally attracting filaments. A very detailed model in three dimensions in the presence of polymerization, steric interactions, and angular stiffness of the filament-CL bond (20) revealed how the morphology of the bundled network scales with mechanical and biochemical parameters. Last, but not least, a combination of scaling estimates and Brownian dynamics simulations with simplified CL properties revealed multi-scale transitions from the isotropic to bundled phase (11). Most of these previous studies focused on the actin network structure rather than on the temporal evolution of the bundled state.

In this paper, we use agent-based simulations to quantify the evolution of the clustered bundle state from a homogeneous meshwork of filaments and examine the role of Brownian motion therein. We begin by describing our computational methods (3,21). Then, we demonstrate how a composite bundle state, and subsequently a clustered bundle state, evolve from a homogeneous meshwork, similar to what is observed in experimental networks (4). We introduce a timescale, τ_c, that quantifies the time to reach the composite bundle state and show that the dynamics on shorter, but not so much on longer, timescales are accelerated by Brownian motion. Although we do not consider steric interactions, we demonstrate that the strong cross-linking present at later times is sufficient to arrest the bundling process. We also show that the bundling timescale is limited by filament diffusion for smaller CL concentrations, although for larger CL concentrations, this diffusion has a minor effect. We find that the relative CL-to-actin ratio required to achieve the same bundling time decreases with increasing actin network mesh size. Finally, we show that the diffusion effect explains the faster bundling for shorter filaments. We discuss some remaining questions, and possible extensions of our model necessary to answer them, in the conclusions.

MATERIALS AND METHODS

We begin with a review of the kinematics of inextensible fibers, slender body hydrodynamics, and our model of dynamic cross-linking (3,21). In our model, actin fibers are represented by one-dimensional curves whose shape, position, and orientation evolve over time under the action of a network of dynamic CLs. The CLs are modeled as elastic springs between appropriately separated filament pairs and are dynamic because they appear and disappear with characteristic rates. Steric interactions are neglected, as is the chirality and twist elasticity of the actin filaments, and our model does not track CLs as individually diffusing entities. Having studied the role of

hydrodynamics in detail in previous work (3), in this paper, we neglect hydrodynamic interactions between distinct filaments. Lastly, when Brownian motion is included, the filaments are approximated as rigid and bending fluctuations are neglected, since the persistence length of actin (22) is at least 10 times the length of the fibers we consider.

After reviewing our formulation from previous work (3,21), we introduce new material pertinent to the simulation of actin bundles, including how we modify our algorithm to simulate rigid fibers and to account for their translational and rotational diffusion. Once we introduce thermal motion, a consistent model also requires us to keep the CL dynamics in detailed balance, i.e., that the binding and unbinding dynamics are in equilibrium with respect to the Gibbs-Boltzmann distribution. We account for this via a simple change to the rates of CL binding. Finally, we discuss how we use a time-splitting algorithm to evolve the system in time. Although the CL binding and unbinding dynamics and filament evolution are treated in a first-order-accurate manner, we use a higher order integrator for the Brownian term that can more accurately preserve fluctuation-dissipation balance.

Dynamic cross-linking of semiflexible, inextensible fibers

This section reviews our algorithm for simulating the dynamic cross-linking of semiflexible fibers (3,21), beginning with the kinematics of inextensible fibers and slender-body hydrodynamics (21) and concluding with our model of dynamic cross-linking (3). As in our previous work (3,21), we use a periodic boundary condition in all three dimensions to mimic a bulk suspension.

Semiflexible, inextensible fibers

We represent the centerline of each fiber by the Chebyshev interpolant $\boldsymbol{X}(s)$, where $s\in[0,L]$ is arclength and L is the fiber length. Likewise, the corresponding fiber tangent vector is represented by $\boldsymbol{\tau}(s) = \boldsymbol{X}_s(s)$. Because the fibers are inextensible, the tangent vector should have unit length for all time, $\boldsymbol{\tau}(s,t)\cdot\boldsymbol{\tau}(s,t) = 1$, for all s and t. Differentiating this constraint with respect to time, we obtain $\boldsymbol{\tau}_t\cdot\boldsymbol{\tau} = 0$, so that the velocity of the filament centerline can be parameterized as (21)

$$\begin{aligned}\boldsymbol{U}(s) = \boldsymbol{X}_t(s) &= \overline{\boldsymbol{U}} + \int_0^s (\alpha_1(s')\boldsymbol{n}_1(s') + \alpha_2(s')\boldsymbol{n}_2(s'))\,ds' : \\ &= (\mathcal{K}[\boldsymbol{X}]\boldsymbol{\alpha})(s),\end{aligned} \tag{1}$$

where $\boldsymbol{\tau}(s), \boldsymbol{n}_1(s), \boldsymbol{n}_2(s)$ are an orthonormal coordinate system at each s and $\alpha_1(s)$ and $\alpha_2(s)$ are two unknown functions. Eq. 1 defines a continuum kinematic operator $\mathcal{K}$ that parameterizes the space of inextensible motions (Sec. 3 in (21)).

To close the system and solve for $\boldsymbol{\alpha} = \{\alpha_1, \alpha_2, \overline{\boldsymbol{U}}\}$, we need to state the forces acting on the fiber centerline. To enforce the inextensibility constraint, we introduce a Lagrange multiplier force density $\boldsymbol{\lambda}(s,t)$. In addition to the constraint force, the fibers are also subject to a bending force with density $\boldsymbol{f}^{\kappa}[\boldsymbol{X}] = -\kappa\boldsymbol{X}_{ssss}$, where κ is the bending stiffness, and an external force density that comes from any attached cross-links, denoted by $\boldsymbol{f}^{(\mathrm{CL})}$. The total force density at every instant in time is therefore $\boldsymbol{f} = \boldsymbol{\lambda} + \boldsymbol{f}^{\kappa} + \boldsymbol{f}^{(\mathrm{CL})}$. Introducing the hydrodynamic mobility operator $\mathcal{M}[\boldsymbol{X}]$ that gives velocity from force (density), the evolution equation of the fiber centerline can be written as

$$\begin{aligned}\mathcal{K}[\boldsymbol{X}]\boldsymbol{\alpha} &= \mathcal{M}[\boldsymbol{X}]\left(\boldsymbol{f}^{\kappa}[\boldsymbol{X}] + \boldsymbol{\lambda} + \boldsymbol{f}^{(\mathrm{CL})}\right), \\ \mathcal{K}^*[\boldsymbol{X}]\boldsymbol{\lambda} &= 0,\end{aligned} \tag{2}$$

subject to the "free fiber" boundary conditions (23).

$$\begin{aligned}\boldsymbol{X}_{ss}(s=0,t) &= \boldsymbol{X}_{sss}(s=0,t) = 0, \\ \boldsymbol{X}_{ss}(s=L,t) &= \boldsymbol{X}_{sss}(s=L,t) = 0.\end{aligned} \tag{3}$$

We solve Eq. 2 for the kinematic coefficients $\boldsymbol{\alpha}$ and constraint forces $\boldsymbol{\lambda}$. The adjoint condition $\mathcal{K}^*\boldsymbol{\lambda} = 0$ closes the system of equations, and encodes the principle of virtual work that constraint forces $\boldsymbol{\lambda}$ do no work for any inextensible motion of the fiber centerline (Sec. 3.4 in (21)). We still have to discuss the evaluation of $\mathcal{M}[\boldsymbol{X}]$ and $\boldsymbol{f}^{(\mathrm{CL})}$, which we do next.

Mobility evaluation

In previous work (3,21), we utilized three different approaches to evaluate the mobility operator $\mathcal{M}[\boldsymbol{X}]$. All of these approaches are based on traditional slender-body theories (24,25), which relate the velocity of a slender filament in Stokes flow to the force density exerted on its centerline. The total velocity at a point on the filament can be broken into three parts: that from force concentrated near the point (the "local drag" part, which dominates as the fiber becomes infinitely slender), that from the rest of the filament (intra-fiber hydrodynamics), and that from forcing on other filaments (through hydrodynamic interactions mediated by the fluid medium). The first two of these are simple to evaluate, given that they can be computed on each filament separately, but the third is expensive to compute because it involves all-to-all interactions through the fluid.

We have already studied the role of nonlocal hydrodynamic interactions in previous work (3), where we found that the time required to reach a particular bundled state is underestimated by at most $10\% - 20\%$ when inter-fiber hydrodynamic interactions are dropped. In this paper, our interest will be in how parameters other than hydrodynamic interactions affect the bundling time. Therefore, to improve computational efficiency, we will ignore hydrodynamic interactions between distinct filaments and evaluate the mobility by including only the local drag part and intra-fiber hydrodynamics. Specifically, the mobility operator on each fiber is given by nonlocal slender-body theory (24,25).

$$\begin{aligned}(8\pi\mu)\boldsymbol{U}(s) = (8\pi\mu)(\mathcal{M}[\boldsymbol{X}]\boldsymbol{f})(s) = &\left(c(s)\left(\boldsymbol{I} + \boldsymbol{\tau}(s)\boldsymbol{\tau}^T(s)\right)\right. \\ &\left. + \left(\boldsymbol{I} - 3\boldsymbol{\tau}(s)\boldsymbol{\tau}^T(s)\right)\right)\boldsymbol{f}(s) \\ &+ \int_0^L \left(\left(\frac{\boldsymbol{I} + \widehat{\boldsymbol{r}}(s,s')\widehat{\boldsymbol{r}}^T(s,s')}{r(s,s')}\right)\boldsymbol{f}(s')\right. \\ &\left. - \left(\frac{\boldsymbol{I} + \boldsymbol{\tau}(s)\boldsymbol{\tau}^T(s)}{|s-s'|}\right)\boldsymbol{f}(s)\right)ds',\end{aligned} \tag{4}$$

where $\boldsymbol{r}(s,s') = \boldsymbol{X}(s) - \boldsymbol{X}(s')$, $r = \|\boldsymbol{r}\|$, $\widehat{\boldsymbol{r}} = \boldsymbol{r}/r$, and $c(s)$ is a local drag coefficient, which has a logarithmic dependence on the fiber radius a. Away from the fiber endpoints, we use the classical result (24).

$$c(s) = \ln\left(\frac{4(L-s)s}{a^2}\right). \tag{5}$$

Near the endpoints, we regularize Eq. 5 over a distance $\delta = 0.1L$, as discussed in (Sec. 2.1 in (21)). The choice of mobility in Eq. 4 allows us to simulate the evolution of bundles faster and prevents possible numerical problems that could result when evaluating the nonlocal flows induced by hundreds of filaments in a bundle on each other (3).

Evaluation of $\boldsymbol{f}^{(\mathrm{CL})}$

We use a stochastic simulation algorithm to update the locations of the dynamic CLs. At each time step, this algorithm, which we discuss in the next section, gives the fiber indices i and j that are linked by each link, as well as the arclength coordinates s_i^* on fiber i and s_j^* on fiber j, where the link is

bound. Letting K_c be the link stiffness (units force/length) and ℓ the CL rest length, we define the force density on fiber i due to the CL as

$$\boldsymbol{f}_i^{(\mathrm{CL})}(s) = -K_c\left(1-\frac{\ell}{\|\boldsymbol{X}^{(i)}(s_i^*)-\boldsymbol{X}^{(j)}(s_j^*)\|}\right)\delta_h\left(s-s_i^*\right)\int_0^L\left(\boldsymbol{X}^{(i)}(s)-\boldsymbol{X}^{(j)}(s')\right)\delta_h\left(s'-s_j^*\right)\,ds', \tag{6}$$

where δ_h is a Gaussian density with standard deviation σ. Although $\sigma\to 0$ corresponds to a standard spring point force, we use a finite σ to preserve smoothness for our spectral numerical method. For $N=16$ points per fiber, which we use throughout this paper, we use $\sigma/L=0.1$ (21). As discussed in (3), this model is an approximation to the complex elasticity of α-actinin and is based on experimental observations that the torsional stiffness of the α-actinin-actin bond does not influence the dynamics of that bond (26).

Dynamic cross-linking

Our model of dynamic cross-linking is discussed in detail in (3). Briefly, we discretize each fiber into N_u uniformly spaced "binding sites" with distance $\Delta s_u = L/(N_u-1)$ between the sites. We make the assumption that the diffusion of individual CLs is sufficiently fast that it can be coarse grained into a single binding rate k_{on} with units 1/(length $\times$ time). This means that a CL end can bind to a single discrete fiber-binding site with rate $k_{\mathrm{on}}\Delta s_u$ per second. In the absence of Brownian motion, as in (3), when one end of the CL is bound, the second end can bind to a nearby fiber with rate $k_{\mathrm{on},s}$. By "nearby" we mean a binding site on a distinct fiber that is within a distance interval

$$(\ell-\delta l,\ell+\delta l),\quad \text{where}\quad \delta\ell=\sqrt{\frac{kT}{K_c}} \tag{7}$$

from the first bound end, where ℓ is the CL rest length and $\delta\ell$ is a measure of the fluctuations in spring length.

Each of the binding reactions has a reverse reaction: a CL with both ends bound can have one end unbind, leaving one end bound, with rate $k_{\mathrm{off},s}$, and a CL with one end bound can unbind with rate k_{off} to have zero ends bound. There are thus four possible reactions, which we simulate stochastically using a version of the standard stochastic simulation/Gillespie algorithm (27,28). The details of our implementation can be found in (3).

In the clustered bundle states that we simulate here, the number of links attached to a given site can grow without bound. To prevent this, we introduce a CL width $c_w = 20$ nm (29) and set the maximum number of bound CLs at each site to $\lceil \Delta s_u/c_w\rceil$. We implement this in the stochastic simulation algorithm using rejection: if a binding event is selected and the binding site is full, we simply move on to the next possible event.

Modifications for rigid fibers

To straightforwardly account for thermal fluctuations, we will consider the case when the fibers are rigid, so that the only possible fluctuations are translational and rotational diffusion. To simulate rigid fibers, we modify the kinematic operators $\mathcal{K}[\boldsymbol{X}]$ and $\mathcal{K}^*[\boldsymbol{X}]$ in Eqs. 1 and 2. For rigid fibers, we introduce $\boldsymbol{\alpha}\equiv\boldsymbol{V}=\{\boldsymbol{U}_c,\boldsymbol{\Omega}\}$ to parameterize the space of rigid body motions, where $\boldsymbol{U}_c = d\boldsymbol{X}_c/dt$ is the translational velocity of the fiber center $\boldsymbol{X}_c=\boldsymbol{X}(L/2)$ and $\boldsymbol{\Omega}$ is the angular velocity of the fiber about its center. This gives the fiber velocity

$$\boldsymbol{U}(s) = (\mathcal{K}_r\boldsymbol{V})(s) = \boldsymbol{U}_c+\boldsymbol{\Omega}\times(\boldsymbol{X}-\boldsymbol{X}_c), \tag{8}$$

which reduces the constraint of virtual work to the fact that $\boldsymbol{\lambda}$ produces no net force and torque,

$$\mathcal{K}_r^*\boldsymbol{\lambda} = \begin{pmatrix}\int_0^L \boldsymbol{\lambda}(s)\,ds\\ \int_0^L(\boldsymbol{X}(s)-\boldsymbol{X}_c)\times\boldsymbol{\lambda}(s)\,ds\end{pmatrix} = 0. \tag{9}$$

We then solve the system (2) with $\mathcal{K}_r$ and $\mathcal{K}_r^*$ replacing $\mathcal{K}$ and $\mathcal{K}^*$. In the supporting text, we show how to easily generalize our discretization for inextensible fibers (21) to straight rigid fibers by restricting the number of Chebyshev modes included in the kinematic operator $\mathcal{K}$ to only the first one.

Because the fibers are rigid, we can formulate the hydrodynamic mobility as a 6×6 mobility matrix $\boldsymbol{N}[\boldsymbol{X}]$, which computes the fiber motion due to a total force $\boldsymbol{F}$ and torque $\boldsymbol{T}$,

$$\boldsymbol{V}=\begin{pmatrix}\boldsymbol{N}_{\mathrm{tt}} & \boldsymbol{N}_{\mathrm{tr}}\\ \boldsymbol{N}_{\mathrm{rt}} & \boldsymbol{N}_{\mathrm{rr}}\end{pmatrix}\begin{pmatrix}\boldsymbol{F}\\ \boldsymbol{T}\end{pmatrix}=\boldsymbol{N}\begin{pmatrix}\boldsymbol{F}\\ \boldsymbol{T}\end{pmatrix}. \tag{10}$$

When the fibers are straight, as in this work, and we measure the mobility about the geometric center of the fiber, the cross translation-rotation and rotation-translation mobilities vanish, $\boldsymbol{N}_{\mathrm{tr}}=\boldsymbol{N}_{\mathrm{rt}}=0$. We recall that, in this work, we neglect hydrodynamic interactions between fibers, so the mobility matrix $\boldsymbol{N}$ can be computed for each fiber separately.

The mobility $\boldsymbol{N}$ can be obtained numerically from the slender-body mobility matrix $\boldsymbol{M}$ (see Sec. 4.2 in (21) for the discretization) via the Schur complement (30,31)

$$\boldsymbol{N}=\left(\boldsymbol{K}_r^*\boldsymbol{M}^{-1}\boldsymbol{K}_r\right)^{\dagger}. \tag{11}$$

Note that the pseudo-inverse is required because applying a torque about the axis of a straight fiber produces no net motion (other than twisting, which we do not account for here). For straight fibers with constant tangent vector $\boldsymbol{\tau}$, by symmetry, the mobility $\boldsymbol{N}$ must be of the form

$$\boldsymbol{N}_{\mathrm{tt}}=\frac{1}{\mu L}(\alpha(\varepsilon)\boldsymbol{I}+\beta(\varepsilon)\boldsymbol{\tau}\boldsymbol{\tau}),\quad \boldsymbol{N}_{\mathrm{rr}}=\frac{\gamma(\varepsilon)}{\mu L^3}(\boldsymbol{I}-\boldsymbol{\tau}\boldsymbol{\tau}). \tag{12}$$

In Table S1, we tabulate the coefficients α,β, and γ for biologically relevant ε. See also (32) for semi-analytical approximations.

Thermal fluctuations with rigid fibers

For Brownian dynamics simulations, we need to solve the overdamped Ito Langevin equation

$$\begin{aligned}\frac{\partial\boldsymbol{X}}{\partial t} &= \mathcal{M}\left(\boldsymbol{\lambda}+\boldsymbol{f}^{(\mathrm{CL})}\right)+\sqrt{2k_BT}\,\mathcal{K}_r\boldsymbol{N}^{1/2}\mathcal{W},\\ &= \mathcal{K}_r\boldsymbol{N}\mathcal{K}_r^*\boldsymbol{f}^{(\mathrm{CL})}+\sqrt{2k_BT}\,\mathcal{K}_r\boldsymbol{N}^{1/2}\mathcal{W}\end{aligned} \tag{13}$$

where $\mathcal{W}(t)$ is a vector of six independent and identically distributed white-noise processes and $\boldsymbol{N}^{1/2}(\boldsymbol{N}^{1/2})^T=\boldsymbol{N}$. The last equality, which puts the overdamped Langevin equation into the more traditional symmetric form, follows from the fact that the deterministic velocity can be written using Eqs. 9 and 10 as

$$\begin{aligned}\boldsymbol{U} &= \mathcal{M}\left(\boldsymbol{\lambda}+\boldsymbol{f}^{(\mathrm{CL})}\right) = \mathcal{K}_r\boldsymbol{V}\\ &= \mathcal{K}_r\boldsymbol{N}\mathcal{K}_r^*\left(\boldsymbol{\lambda}+\boldsymbol{f}^{(\mathrm{CL})}\right) = \mathcal{K}_r\boldsymbol{N}\mathcal{K}_r^*\boldsymbol{f}^{(\mathrm{CL})}.\end{aligned} \tag{14}$$

Note that, because the fiber mobility is measured around the obvious geometric center, there is no stochastic drift term in the resulting Ito overdamped Langevin Eq. 13 (33,34). In our Brownian dynamics simulations with straight fibers, we use the precomputed values of α, β, and γ in

Eq. 12 to generate $N_{tt}^{1/2}$ and $N_{rr}^{1/2}$ from the fiber tangent vector $\boldsymbol{\tau}$ according to Eq. S10 in the supporting text.

The random displacement of a fiber over a time interval τ can be sampled the following way:

1. Draw a vector $\boldsymbol{W}$ of six independent and identically distributed standard Gaussian variates and sample the rigid velocity,

$$\begin{pmatrix} \boldsymbol{U}_c \\ \boldsymbol{\Omega} \end{pmatrix} = \sqrt{\frac{2k_BT}{\tau}}\boldsymbol{N}^{1/2}\boldsymbol{W}. \tag{15}$$

2. Update the fiber by translating its center by $\boldsymbol{U}_c\tau$ and rotating the fiber about its center by an oriented angle $\boldsymbol{\Omega}\tau$.

Note that, for straight fibers, one can simplify the formulation of Brownian dynamics; the formulation presented here applies to curved rigid fibers as well.

Keeping the CL dynamics in detailed balance

When we account for thermal translation and rotation of the fibers, we also want to be sure that the binding and unbinding of the links is consistent with detailed balance, which is not the case for the constant rates we introduced earlier. Let $\boldsymbol{C}$ denote a configuration of C links (list of fiber pair connections) and $\boldsymbol{x}$ denote the configuration of fibers (binding site positions). The desired Gibbs-Boltzmann equilibrium distribution is

$$P_{\text{eq}}(\boldsymbol{C},\boldsymbol{x}) = \zeta(\boldsymbol{C})\prod_{k\in\boldsymbol{C}}\exp\left(-\frac{K_c}{2}\frac{(\ell_k-\ell)^2}{k_BT}\right), \tag{16}$$

where ℓ_k is the length of link k and $\zeta(\boldsymbol{C})$ determines the probability to observe the cross-linking configuration $\boldsymbol{C}$. Now consider a transition to or from a state $\boldsymbol{C}'$ with one added link C', which has length ℓ_k'. Then, at equilibrium, the transition between the two states must obey

$$P_{\text{eq}}(\boldsymbol{C},\boldsymbol{x})k_{\text{on,s}}(\ell_k') = P_{\text{eq}}(\boldsymbol{C}',\boldsymbol{x})k_{\text{off,s}}(\ell_k'). \tag{17}$$

Substituting P_{eq} from Eq. 16 into Eq. 17, we obtain the constraint of detailed balance

$$\frac{k_{\text{on,s}}(\ell_k')}{k_{\text{off,s}}(\ell_k')} = \frac{\zeta(\boldsymbol{C}')}{\zeta(\boldsymbol{C})}\exp\left(-\frac{K_c}{2}\frac{(\ell_k'-\ell)^2}{k_BT}\right). \tag{18}$$

To satisfy Eq. 19 for every choice of $\boldsymbol{C}$ and $\boldsymbol{C}'$ with binding and unbinding rates that only depend on spring length and not $\boldsymbol{C}$ and $\boldsymbol{C}'$, we must have

$$\frac{k_{\text{on,s}}(\ell_k')}{k_{\text{off,s}}(\ell_k')} = \frac{k_{\text{on,s}}^0}{k_{\text{off,s}}^0}\exp\left(-\frac{K_c}{2}\frac{(\ell_k'-\ell)^2}{k_BT}\right), \tag{19}$$

where $k_{\text{on,s}}^0$ and $k_{\text{off,s}}^0$ are the transition rates for a link at rest length.

To satisfy Eq. 19, we maintain a constant $k_{\text{off,s}}(\ell_k') = k_{\text{off,s}}^0$ and set

$$k_{\text{on,s}}(\ell_k') = k_{\text{on,s}}^0\exp\left(-\frac{K_c}{2}\frac{(\ell_k'-\ell)^2}{k_BT}\right). \tag{20}$$

Other choices are possible; for example, the rate of unbinding can depend on the stretch (35,36). To efficiently search for possible binding pairs, we approximate the set of all binding combinations by setting the maximum link stretch in Eq. 7 to be two standard deviations of the Gaussian in Eq. 20, i.e., $\delta\ell = 2\sqrt{k_BT/K_c}$.

Temporal integration

We employ a time-splitting approach to evolve the cross-linked actin network. At each time step, we have three processes to simulate: the thermal diffusion of the fibers, the binding and unbinding of the dynamic CLs, and the deterministic evolution of the fiber positions. The last two of these steps are laid out in full in (3), where we employ Lie splitting to first process binding and unbinding events and then use the method developed in (21) to evolve the fiber positions in an inextensible (or rigid; see supporting text section A) way. Here, we use the first-order accurate, backward Euler version of the deterministic fiber update, which is discussed in (3).

It remains to be determined how we will treat the Brownian update. We use a second-order Strang-type splitting scheme, where during each time step of duration Δt we:

1. Randomly displace and rotate the fibers over a time interval $\tau = \Delta t/2$ using the algorithm around Eq. 15.
2. Update the cross-link attachments (using the stochastic simulation algorithm) and perform a deterministic fiber update, both over a time interval Δt, using the method of (3).
3. Randomly displace and rotate the fibers over a time interval $\tau = \Delta t/2$ using the algorithm around Eq. 15.

Network statistics

We quantify the evolution of the cross-linked actin network by examining the connectivity of the fibers in two ways. First, given the total number of CLs in the system C, we compute an average link density per fiber via the formula "Link density" $= 2C/(LF)$. Second, we map the network to a connected graph to study how the structure evolves in time (13). We define a "bundle" as a connected group of at least $F_B = 2$ filaments, where a connection between two fibers is a pair of links with anchoring locations at least $d_{\text{bund}} = L/4$ apart on each fiber (3), so that the links limit the fibers' rotational degrees of freedom. We then define two measures of the degree of bundling in the system. The first measure is the bundle density, which is the number of bundles per unit volume B/L_d^3, where B is the number of bundles and L_d is the length of the simulation cell. The second measure is the percentage of fibers in bundles, defined as the percentage of filaments connected to at least one other filament by two links at least $d_{\text{bund}} = L/4$ apart. The bundle density statistic preferentially weights smaller bundles, since a bundle of two filaments is counted the same as a bundle of five filaments, although the percentage of fibers in bundles is independent of F_B (one can think of a bundle of F_B filaments as contributing a weight $\sim 1/F_B$ to the bundle density but a weight $\sim F_B$ to the percentage of fibers in bundles.)

For a bundle of b filaments, we define an orientation parameter as the maximum eigenvalue of the matrix (13).

$$\boldsymbol{Q} = \frac{1}{bL}\sum_{i=1}^{b}\int \boldsymbol{\tau}^{(i)}(s)\left(\boldsymbol{\tau}^{(i)}(s)\right)^T ds. \tag{21}$$

The orientation parameter takes values in $[1/3, 1]$, with 1 being the value for a group of straight fibers with the same tangent vector. Given information about the bundles, we compute an average bundle orientation parameter by taking an average over bundles with at least two filaments, weighted by the number of filaments in each bundle.

Throughout this paper, we will quantify the concentration of fibers in terms of the initial mesh size (37) of the suspension, $\ell_m = \sqrt{L_d^3/(FL)}$ (parameters are defined in Table 1). Note that this estimate for ℓ_m applies to non-bundled (disordered) suspensions of fibers, so really when we use ℓ_m, we mean the *initial* mesh size, before the bundling process beginning. We will operate in the regime where the fluctuations in the CL rest length as defined in Eq. 7, which are of magnitude $\delta\ell = 20$ nm (see parameters in Table 1), are several times smaller than the typical filament spacing, which

TABLE 1 Simulation parameters

Parameter	Definition	Value	Unit	Notes
a	fiber radius	4	nm	(38)
L	fiber length	0.5, 1	μm	(39,40)
F	number of fibers	200–1,600		
L_d	simulated volume's extent	2–4	μm	cubic unit cell
μ	cytoplasm viscosity	0.1	Pa•s	100 × water (cytoplasm) (41)
κ	fiber bending stiffness	0.07	pN•μm^2	17 μm persistence length (22)
K_c	CL spring stiffness	10	pN/μm	(42)
ℓ	CL rest length	50	nm	(29)
k_{on}	CL first end binding rate	5	1/(μm•s)	(3)
$k_{\text{on,s}}$	CL second end binding rate	50	1/(μm•s)	$k_{\text{on,s}} \gg k_{\text{on}}$, not measured
k_{off}	CL (one end bound) unbinding rate	1	1/s	(43,44)
$k_{\text{off,s}}$	CL (both ends bound) unbinding rate	1	1/s	$k_{\text{off,s}} = k_{\text{off}}$
c_w	actin-binding site width	20	nm	(29)
k_BT	thermal energy	4×10^{-3}	pN•μm	25°C
N	number of Chebyshev points	16		((21), Sec. 6.3.1)
Δs_u	binding site spacing	0.026	μm	(3)
Δt	time step size	10^{-4}	s	limited by K_c

is at most the initial mesh size $\ell_m = \mathcal{O}(100)$ nm and at least the cross-linker length of 50 nm.

RESULTS AND DISCUSSION

We begin this section by discussing the kinetics of bundling for non-Brownian, semiflexible fibers and establish that semiflexible fibers with a persistence length similar to that of actin (22) can be well approximated by rigid filaments. We then show that rigid, Brownian fibers have similar kinetic behavior, except that the Brownian motion (translational and rotational diffusion) speeds up the timescale of bundling.

After these preliminaries, we use our simulations to clarify and explain some of the experimental results on the dynamic formation of cross-linked actin bundles. First, we show how the timescale needed to reach the composite bundle state depends on the fiber concentration (initial mesh size) and concentration of CLs (which controls k_{on} in our model). We show that the bundling process is slower when the actin or CL concentration is lower but that bundling can still occur at low actin concentration, provided there are enough CLs available to bundle the fibers, and that the relative amount of CLs needed for a fixed bundling time decreases as actin concentration increases. Second, we show that the experimental result that bundling occurs faster for shorter fibers (10,12) can only be reproduced in systems where we consider translational and rotational diffusion. Unless otherwise noted, we will use the simulation parameters listed in Table 1. As discussed in (3), the cross-linking parameters are chosen to mimic α-actinin, although we will compare our results with systems with different CLs, such as filamin (5).

Kinetics of bundling for non-Brownian, semiflexible fibers

We begin with simulations in a system of initial mesh size $\ell_m = 0.2$ μm, which translates to $F = 200$ filaments in an $L_d = 2$ μm domain, $F = 675$ filaments in an $L_d = 3$ μm domain, and $F = 1{,}600$ filaments in an $L_d = 4$ μm domain. The mesh size we use is of the same order of magnitude as that in cell cortex in vivo (45) and corresponds to 10–15 μM G-actin concentration often used in in vitro experiments (8,9). In Fig. S2, we show that the statistics of the bundling process are insensitive to the domain size up to the point where there is mass coalescence of almost all the fibers in the simulation cell. For this reason, we will consider results from only one set of simulations, the one with $F = 675$ filaments and $L_d = 3$.

We initialize the set of F filaments with random locations and orientations and then, during each time step, we evolve the fibers by updating the dynamic CLs and then updating the fiber positions in sequential order. Fig. 1 shows how the bundling process evolves in small and large systems. On the microscopic scale, filaments that are initially not parallel are linked by CLs, which pull them closer together and allow more links to bind. The binding of additional links leads to the alignment of filaments. Note that the key to the bundling process is the flexibility of the CL, in particular, rapid thermal fluctuation of the CL length, which is present implicitly in our model from Eq. 7. Because the CLs are small, fluctuations in their length occur on a timescale that is much faster than other characteristic timescales, and so we do not model the fluctuations explicitly. The combination of the CLs' elasticity and length fluctuations is crucial, as the length fluctuations effectively allow the CLs to "find" the neighboring fibers and bind them, whereupon the elasticity of the CL aligns the fibers, making further cross-linking faster.

This process plays out on a larger scale in snapshots from the simulations, shown in Fig. 1 at $t = 5$, 10, 20, and 40 s. The initial stage of bundling (first two snapshots) is characterized by bundles of a few straight, aligned filaments, which is similar to the experimentally observed composite bundle state (4) and the three-filament bundle shown at the top of Fig. 1. Later times (bottom two frames) show coalescence of these smaller bundles into larger bundles, with

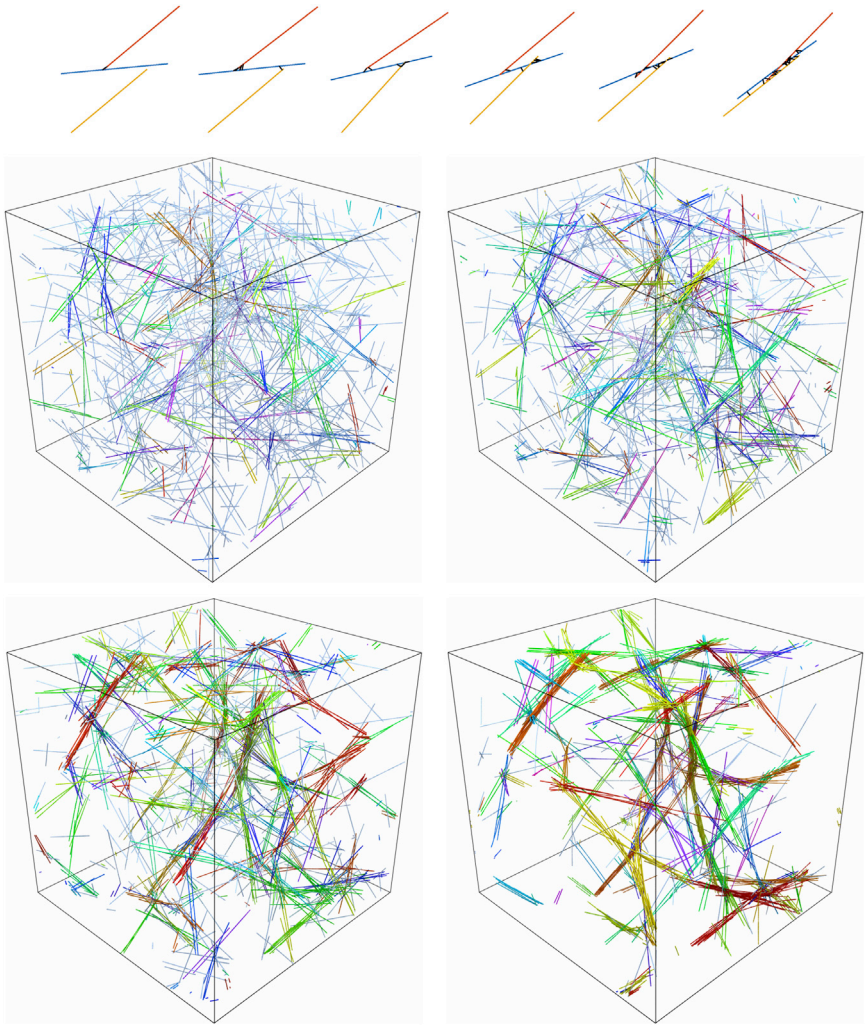

FIGURE 1 Bundling dynamics on small and large scales. Top: a small-scale bundling process with three filaments and snapshots taken at times $t = 0$, 2, 4, 6, 8, and 10 s. Bottom: snapshots of the bundling process taken (from left to right and top down) at $t = 5$, 10, 20, and 40 s for semiflexible fibers with stiffness $\kappa = 0.07$ pN$\cdot\mu$m^2 are shown. Fibers in the same bundle are colored with the same color. The two networks at the middle are before the coalescence transition time $\tau_c \approx 16$ s, whereas the two networks at the bottom are after the coalescence time. To see this figure in color, go online.

some curvature appearing in the fibers in the final frame. By $t = 40$ s, there are only a few bundles made of coalesced smaller bundles and the network resembles the experimentally observed clustered bundle state (4), which approaches the low energy state consisting of a single aligned bundle (46).

To quantify our observations, in Fig. 2, we plot the mean link density ($2C/(LF)$; see the network statistics section), bundle density (B/L_d^3), percentage of fibers in bundles, mean bundle alignment parameter, and mean and maximum bundle size throughout the bundling process for three values of fiber stiffness: $\kappa = 0.07$ (the value for actin), $\kappa = 0.007$ (fibers 10-fold less stiff), and $\kappa = \infty$ (rigid filaments). In all systems, we see the number of links per fiber grow in time to approach the maximum of $\lceil \Delta s_u / c_w \rceil \times L/\Delta s_u = 80$, whereas the bundle density in all systems exhibits a peak around a critical time $\tau_c \approx 16$ s. At this time, the other panels of Fig. 2 tell us that 60% of the fibers are already in bundles, which have a mean alignment parameter larger than 0.9. Fig. S3 gives a more precise look at the composition of the bundles, which are the same for the three values of stiffness when $t \leq \tau_c$: at $t = \tau_c$, most (>50%) of the fibers are in bundles of size 11 or less, with a small percentage (<10%) in bundles of size 10–20 and the other 40% of the filaments not in bundles at all. Thus, a time τ_c into the bundling process, most of the fibers are in small, highly aligned bundles, as we see in the snapshots in Fig. 1, and the dynamics up to this point are roughly independent of the fiber stiffness. Based on Fig. 1, we can also think of τ_c as the time required to reach the composite bundle state. For this system of non-Brownian filaments, Fig. 2 shows $\tau_c \approx 16$ s corresponds to the timescale of increase of the percentage of fibers in bundles (see middle left frame), meaning it is also the timescale on which the fibers' rotational degrees of freedom are arrested or constrained.

After the coalescence time, we see a transition to coalescence of bundles, and the flexibility of the fibers comes into play. Fig. 2 shows that the number of bundles is declining and the mean bundle alignment is dropping for $t > \tau_c$, which implies that bundles are forming with non-aligned fibers. The mean and maximum bundle sizes also start to grow, which again means that small bundles are coming together

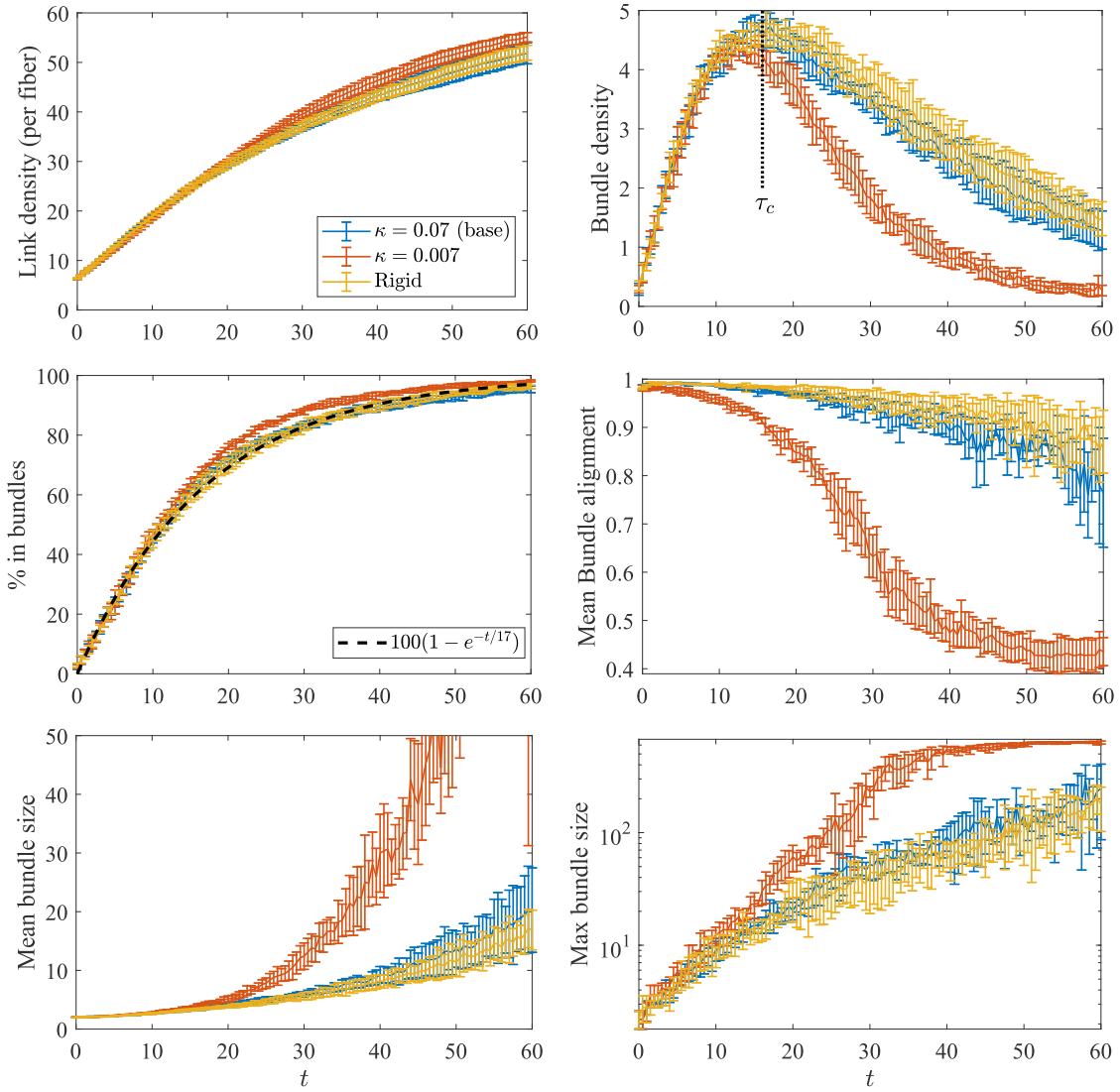

FIGURE 2 Statistics for the bundling process with filaments of varying stiffness. We compare the base parameters ($\kappa = 0.07$ pN$\cdot\mu$m^2, blue) with the systems with smaller bending stiffness ($\kappa = 0.007$, orange) and rigid fibers ($\kappa \to \infty$, yellow). After $\tau_c \approx 16$ s, the bundling dynamics for the less stiff fibers are significantly faster. Fibers with similar bending stiffness to actin are well approximated by rigid fibers. Error bars are the error in the mean over five trials. To see this figure in color, go online.

to form the larger ones we see in the bottom row of Fig. 1. Fig. S3 shows that, by $t = 60$ s, at least 75% of the fibers are in bundles of size 30 or larger. It is in this stage where the flexibility of the fibers can become important: when $\kappa = 0.007$ (fibers 10-fold less stiff than actin), coalescence of bundles occurs faster than in systems with $\kappa = 0.07$ or systems with rigid fibers, since in the former case, the fibers are more compliant and can be linked together more easily by deforming. That said, when $\kappa = 0.07$ (persistence length 17 μm), Figs. 2 and S3 show that the dynamics throughout the bundling process are well approximated by rigid filaments. This analysis is of course limited by the fiber length we have chosen: in particular, we have shown that, in the absence of Brownian motion, rigid filaments are a good approximation to semiflexible actin filaments for fibers of length ≤ 1 μm, which are most common in vivo. The approximation will be worse as the filament length gets larger. Henceforth, we will consider rigid fibers only.

Thermal fluctuations speed up the bundling process

We now consider simulations with rigid fibers, for which we can account for translational and rotational diffusion using standard Brownian dynamics methods (33), while maintaining detailed balance in the cross-linking kinetics. An important quantity in this case is the time for a fiber to diffuse across a mesh size. In our initial set-up, the fibers are spaced approximately ℓ_m apart, and they first must find each other to cross-link and begin the bundling process. The theoretical

translational diffusion coefficient of a straight fiber, derived in (33), can be written in terms of the 3×3 translational mobility matrix $\boldsymbol{N}_{\mathrm{tt}}$ for rigid body motions as

$$D_t = \frac{k_B T}{3}\mathrm{tr}(\boldsymbol{N}_{\mathrm{tt}}) \approx \frac{k_B T}{3\mu L} 1.67, \tag{22}$$

where the last equality gives the result for a fiber aspect ratio of $\varepsilon = 0.004$, which we obtain from slender-body theory with intra-fiber hydrodynamics (see Table S1 and note that this estimate accounts for the anisotropy of the fiber, since $\boldsymbol{N}_{\mathrm{tt}}$ has an eigenvalue in the parallel direction that is twice as large as the perpendicular directions). The mean square displacement of the fiber center is then $\langle r^2(t)\rangle = 6D_t t$. Substituting the parameters in Table 1, we obtain $6D_t \approx 0.13$ $\mu\mathrm{m}^2/\mathrm{s}$, and thus, the time to diffuse a mesh size is given by $\tau_m = \ell_m^2/(6D_t) \approx \ell_m^2/0.13$ s. Since diffusion promotes mixing of the suspension and gives more opportunities for cross-linking, our expectation is that thermal fluctuations should speed up the transition from the homogeneous meshwork to the composite bundle state, where bundles are made of a few fibers that must be close enough together to cross-link. This assumes that the CL concentration is large enough for links to bind as soon as fibers are close enough together; we will analyze this assumption in the next section.

To understand how thermal diffusion affects the bundling process, in Fig. 3, we plot the statistics both with (orange) and without (blue) thermal fluctuations. We see that the entire process is faster with diffusion, as we might expect (see Videos S4 and S5), but the degree of acceleration changes

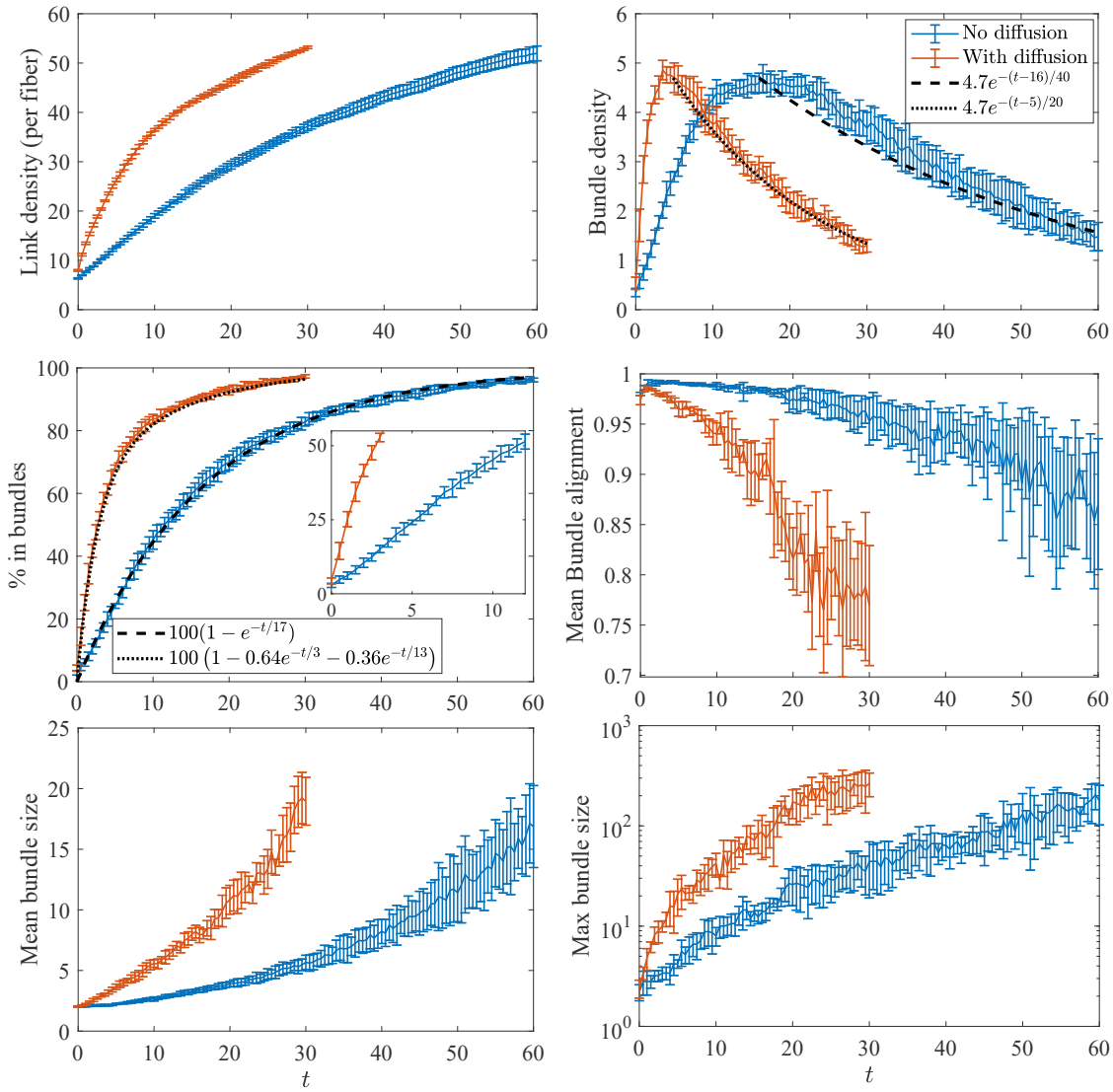

FIGURE 3 Statistics for the bundling process with and without thermal fluctuations. The blue lines show the results without thermal movement, whereas the orange lines show the results with translational and rotational diffusion. Here, we use $\Delta t = 10^{-4}$; we have verified that the statistical noise exceeds the time-stepping error for this time-step size. The peak in the bundle density occurs at $\tau_c \approx 16$ s for systems without diffusion, although for systems with diffusion it occurs at $\tau_c \approx 4$ s. Error bars are the error in the mean over five trials. To see this figure in color, go online.

before and after τ_c. Before τ_c, the process with diffusion is significantly faster than without; for instance, it takes about 3 s for 50% of the fibers to be in bundles with diffusion, whereas without diffusion, it takes 12 s (Fig. 3 inset), which is a difference of a factor of four. Indeed, the critical bundling time $\tau_c \approx 4$ s with diffusion, although we have already seen $\tau_c \approx 16$ s without diffusion, so that the difference is again a factor of four. For $t > \tau_c$, when bundles start to coalesce, the difference is only a factor of two; an exponential fit to the decaying bundle density gives a constant of 20 s for simulations with diffusion and 40 s for simulations without diffusion.

A similar relationship holds when we look not at the number of bundles (which depends on F_B, the minimum number of fibers forming a bundle) but the percentage of fibers in bundles, which is independent of F_B and shown in the middle left frame of Fig. 3. Unlike in the non-Brownian case, where a single timescale fits the data, the Brownian case requires two timescales for fitting, which are 3 s (which is close, but not equal, to $\tau_c \approx 4$ s) and 13 s. In this case, the new fast timescale of 3 s reflects the ability of Brownian filaments to freely diffuse translationally and rotationally early in the simulation. Later in the simulation, the filaments are arrested and the timescale on which filaments enter bundles approaches that of non-Brownian filaments, 17 s. This provides more evidence for our two-stage model of bundling, where thermal fluctuations make more of a difference in the first stage, when fibers are less constrained by CLs. Sure enough, Fig. S4 (*left*, *blue curve*) shows that the mean squared displacement for simulations with Brownian motion decays exponentially to a constant, meaning that, at times larger than τ_c, the Brownian motion is inhibited by cross-linking and therefore becomes less important. Equivalently, entropic effects (Brownian motion of fibers and cross-linker stretching) are more important at early times, whereas at later times, energetic effects trap the fibers in the clustered bundle state.

To show that the network morphology has not changed when we add thermal movement, in Fig. S6, we show the networks at $t \approx \tau_c$ without and with thermal fluctuations. The composite bundle network morphology at τ_c is similar between the two, which demonstrates that fluctuations speed up the pace of bundling without changing the types of bundles that evolve.

In subsequent sections, we will analyze how the timescale τ_c that we use to quantify the speed of bundling depends on the microscopic parameters. Although the precise value of τ_c depends on the parameter F_B (the minimum number of filaments in a bundle), Fig. 3 shows that this timescale can roughly capture the initial growth rate of the percentage of fibers in bundles, which is independent of F_B. Since τ_c is easier to measure by looking at the peak bundle density (and is in principle easier to measure experimentally through microscopy) than by fitting a double-exponential curve (which is an ill-conditioned problem for larger timescales), we will use the bundle density maximum as the definition of τ_c. Of course, making F_B larger increases τ_c, as we show in Fig. S5 by setting $F_B = 5$, but the ratio of τ_c between the Brownian and non-Brownian system remains the same. However, increasing F_B will cause us to miss the initial stage of bundling, where two-filament bundles form and the fibers' rotational degrees of freedom are arrested, so we will use $F_B = 2$ henceforth.

Dependence of bundling timescale on actin and CL concentration

Our conclusion that thermal fluctuations significantly accelerate the initial stage of the bundling process is dependent on having a sufficient concentration of CLs. Although thermal fluctuations undoubtedly increase the frequency of fibers coming close enough together for cross-linking, the bundling process still must be initiated via binding of a CL. Consequently, in this section, we consider a range of values of mesh size (actin concentration) and k_{on} (CL attachment rate, which is proportional to CL concentration) to get a more complete picture of how the critical bundling time τ_c depends on these parameters. In particular, we will consider mesh sizes $\ell_m = 0.2$ ($F = 675$; $L_d = 3$ μm), 0.4 ($F = 400$; $L_d = 4$ μm), and 0.8 μm ($F = 338$; $L_d = 6$ μm) and single-end binding rates $k_{\text{on}} = 1.25$, 5 (the base value), and 20 ($\mu\text{m}\cdot$ s). By changing the rate at which a single CL end binds to a fiber, we effectively vary the CL concentration.

Fig. 4 shows the resulting evolution of the bundle density for the nine different systems, as well as the resulting critical bundling time τ_c. For systems with large k_{on}, where binding is essentially instantaneous once filaments come close enough together, $\tau_c \approx 3$ s for the small-enough mesh sizes of $\ell_m = 0.2$ and 0.4 μm. Once the mesh size increases to 0.8 μm, the bundling time increases but only to about 4.5 s (see inset of Fig. 4). Thus, τ_c is not a strong function of mesh size for larger k_{on}, which implies that the process for large k_{on}, where there is always sufficient cross-linker available for binding, is primarily limited by cross-linking dynamics (alignment of filaments), with diffusion (across the mesh size) playing only a secondary role.

Let us now consider the case of slower k_{on}. In this case, filaments could come close enough to link together but diffuse away before a CL can actually bind them. As a result of this, the bundling process is slowed and, in fact, the peak bundle density drops. Indeed, as shown in Fig. 5, networks with smaller k_{on} (lower CL concentration) contain larger bundles at $t = \tau_c$ than those with larger k_{on} (higher concentration). As shown in Videos S1–S3 upon reducing k_{on}, two filaments finding each other becomes the limiting step in the bundling process. This causes a slow growth of the bundle curve and a bias toward larger bundles, which build up at a faster rate (relative to τ_c), and the process is rate limited by two-filament bundle formation. The scaling of τ_c at small k_{on} (*left column* of the *bottom right* panel in Fig. 4) is reminiscent of a diffusion-limited process, as it increases from

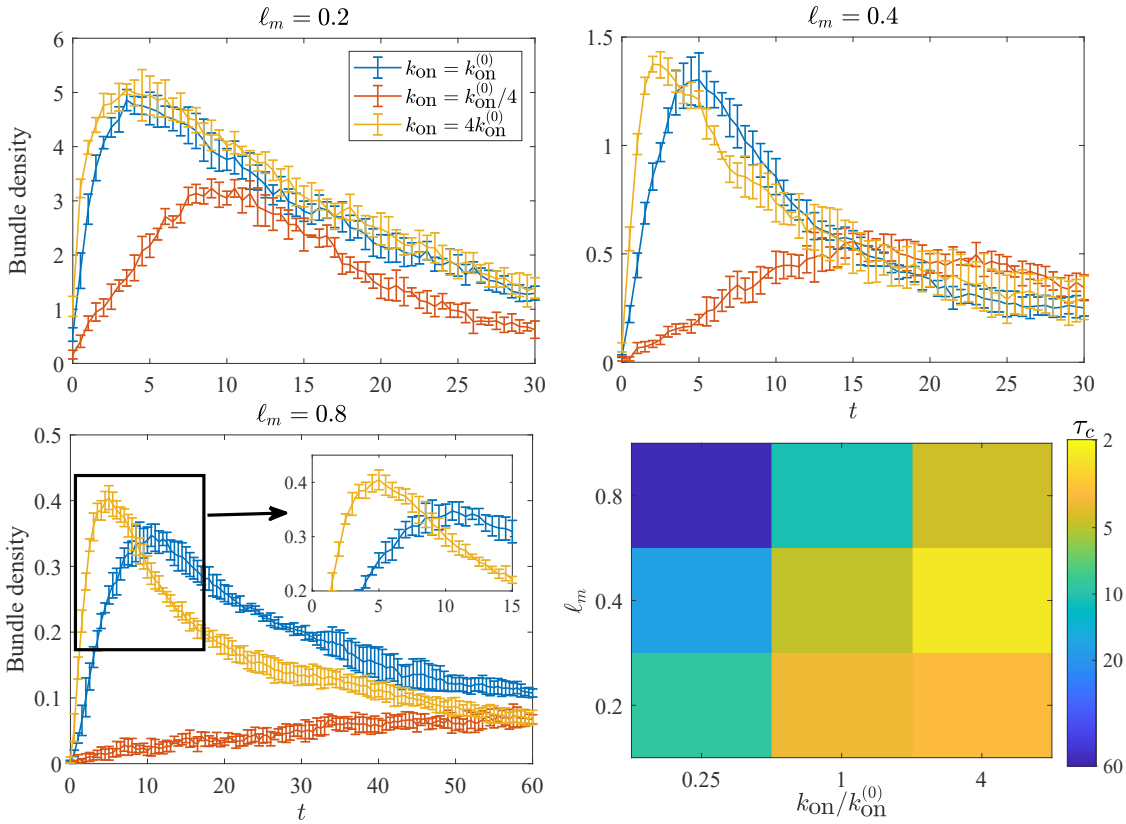

FIGURE 4 Bundling timescales for a range of initial mesh sizes ℓ_m and binding rate k_{on}. The first three frames show the trajectory of the bundle density for the different mesh sizes, where blue lines denote our base value of $k_{on} = k_{on}^{(0)} = 5$ (μm•s), orange lines denote $k_{on}/k_{on}^{(0)} = 1/4$, and yellow lines denote $k_{on}/k_{on}^{(0)} = 4$. Error bars are the error in the mean over five trials. The bottom right frame shows the dependence of the critical bundling time τ_c on ℓ_m and k_{on}. To see this figure in color, go online.

9 s to 17 s, then to 56 s as the mesh size doubles, scaling approximately as ℓ_m^2 as the mesh size increases. In some sense, diffusion is actually a hindrance to bundling, since fibers that are close to each other diffuse away before a CL can bind them together.

We note that a roughly constant bundling time can be achieved by decreasing k_{on} as the mesh size decreases (moving from the *top right* to the *bottom left* of the *bottom right* panel in Fig. 4). This implies that the relative concentration of CL required for a particular bundled state decreases with the mesh size, as has been found experimentally (5). When the mesh size is smaller, the filaments are in contact for longer, and so it is less important that a CL be available immediately to bind them together. By contrast, filaments in larger-mesh-size systems are only in contact for a brief time, so relatively more CLs are necessary to ensure that these filaments are linked when they come into contact with each other.

Brownian motion is responsible for faster bundling with shorter filaments

We will now explore the dependence of the critical bundling time τ_c on the fiber length. Experimentally, it has been shown that shorter filaments bundle faster (10,12), but it is still unclear whether this is due to thermal movements, cross-linking kinetics, or some combination of both. In this section, we show that the experimental results can only be reproduced if we consider thermal movements, so that cross-linking kinetics are not responsible for the speedup in bundling. We use a fixed mesh size of $\ell_m = 0.2$ μm, which translates to $F = 675$ filaments of length $L = 1$ μm in a domain of size $L_d = 3$ μm and $F = 400$ filaments of length $L = 0.5$ μm in a domain of size $L_d = 2$ μm.

In Fig. 6, we show how the bundle density, percentage of fibers in bundles, and mean bundle size evolve for the two different filament lengths both 1) without and 2) with actin diffusion. In Fig. 6 *a*, we see that, in the absence of Brownian motion, the behavior in the two systems is similar, with the peak bundle density occurring in both cases around $\tau_c \approx 15$ s. Furthermore, there is only a mild difference in the percentage of fibers in bundles over time. The mean bundle size is at most twice larger for the system with shorter filaments, but we would expect this, since the filaments are twice as short and there are twice as many of them if ℓ_m is fixed.

Earlier, we showed that Brownian motion speeds up the bundling process by promoting mixing and more near

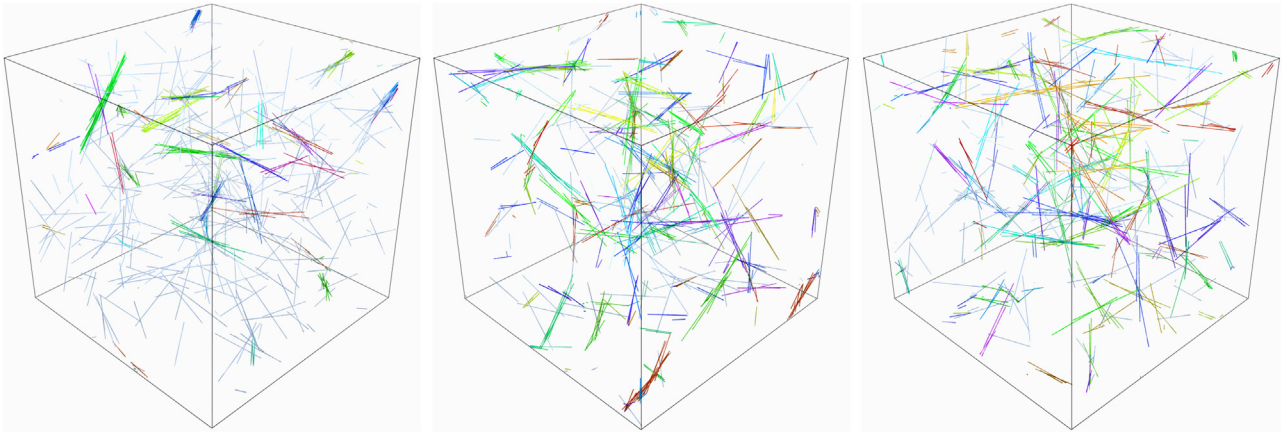

FIGURE 5 Snapshots of the network at $t = \tau_c$ with initial mesh size $\ell_m = 0.4$ μm and varying CL concentration. The networks contain $F = 400$ filaments of length $L = 1$ in a domain of size $L_d = 4$ with $k_{on}/k_{on}^{(0)} = 1/4$ (left, $\tau_c \approx 17$), $k_{on}/k_{on}^{(0)} = 1$ (middle, $\tau_c \approx 5$), and $k_{on}/k_{on}^{(0)} = 4$ (right, $\tau_c \approx 2.5$). A smaller k_{on} (smaller CL concentration) gives fewer but larger bundles at $t = \tau_c$, as well as a smaller percentage of fibers in bundles. To see this figure in color, go online.

contacts of filaments. In particular, we saw that the time for a filament with length $L = 1$ μm to diffuse a mesh size of $\ell_m = 0.2$ μm is $\tau_m \approx 0.30$ s, so that filaments can find each other rapidly and begin the bundling process. In the case of filaments with $L = 0.5$ μm, our thermal diffusion coefficient in Eq. 22 scales log-linearly with the fiber length, so that it takes $\tau_m = 0.17$ s to diffuse a mesh size of $\ell_m = 0.2$ μm. We might expect, therefore, that at least the initial stages of the bundling process will be sped up by a factor of two.

Fig. 6 *b* shows that this is indeed the case. For $\ell_m = 0.2$ μm, the bundle density peak occurs around $\tau_c \approx 2$ s when $L = 0.5$ μm, although with $L = 1$ μm, it occurs around $\tau_c \approx 4$ s, so it appears that bundling time with thermal motion scales linearly with filament length, which is in (approximate) accordance with the scaling of the translational diffusion coefficient. The faster bundling behavior also manifests itself in the link density and percentage of fibers in bundles, where we see that systems with shorter filaments reach a number of links or percentage of fibers about twice as fast. For instance, 80% of the fibers are in bundles by $t \approx 4$ s in the $L = 0.5$ μm case, although with $L = 1$ μm, the 80% mark is not reached until about $t \approx 8$ s.

Ratio of bundling and turnover times control steady-state morphology

Because we define the bundle density in terms of bundles of an arbitrary number of filaments ($F_B = 2$), the precise value of the timescale τ_c that we obtain is also somewhat arbitrary. Indeed, plotting the decay of the fibers' mean-square displacement over the course of the simulation, as we do in Figs. S4 and S7, shows that τ_c is not the only timescale characterizing the bundling process. However, if we increase the number of filaments required for a bundle to $F_B = 5$, Fig. S5 shows that the peak in the bundle density occurs about a factor of two later in both Brownian and non-Brownian filament simulations. We therefore postulate that the ratio $\tau_c^{(A)}/\tau_c^{(B)}$ between systems A and B is a meaningful quantity, approximately independent of the definition of τ_c, and can be used to predict the steady-state morphology in systems with fiber turnover.

To test this, we introduce filament turnover with mean filament lifetime τ_f (see (3) for implementation details) and fix τ_f as a function of τ_c, so that the ratio of the turnover times equals the ratio of the bundling times between the Brownian (B) and non-Brownian (NB) cases, $\tau_f^{(B)}/\tau_f^{(NB)} = \tau_c^{(B)}/\tau_c^{(NB)}$, or equivalently, $\tau_f^{(NB)}/\tau_c^{(NB)} = \tau_f^{(B)}/\tau_c^{(B)}$. In Fig. 7, we vary the ratio τ_f/τ_c between 0.5 and 2 and plot the bundle density and percentage of fibers in bundles as they evolve to a steady state in each case. Despite the system of Brownian filaments having much faster bundling dynamics than the system of non-Brownian filaments, the morphology of the steady state is the same in the Brownian and non-Brownian cases, as is shown in the snapshots of Fig. S8.

CONCLUSION

We used numerical simulations to investigate the kinetics of bundling in cross-linked actin suspensions. After validating that semiflexible actin fibers can be approximated as rigid in non-Brownian suspensions, we treated actin fibers as Brownian rigid, straight, slender rods, in accordance with a number of other simulation studies (11,13). We coarse grained the diffusion and binding and unbinding of α-actinin CLs into four microscopic rates: $k_{on}, k_{on,s}, k_{off}$, and $k_{off,s}$. This enabled the simulation of a gel with about 700 actin fibers and as many as 50 CLs bound to each fiber.

We found that, even without thermal movements, actin filaments can still bundle, as filaments that are initially close enough are linked together at small patches with CLs. These

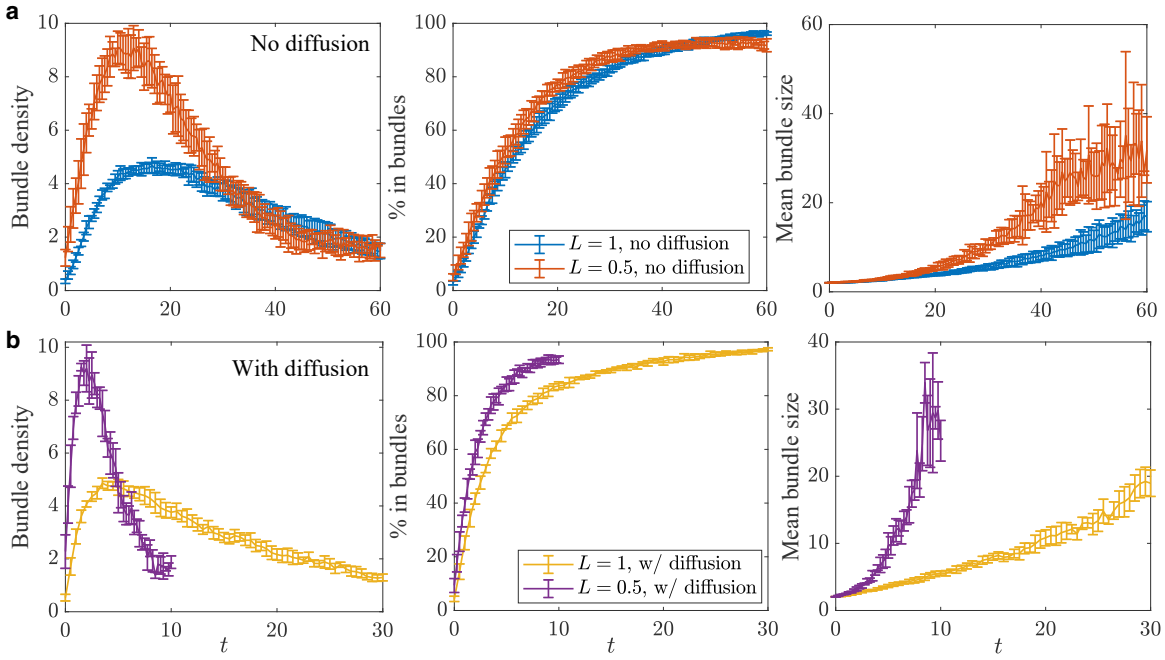

FIGURE 6 Effect of changing filament length for rigid fibers with and without Brownian motion, with constant initial mesh size $\ell_m = 0.2$ μm. (*a*) Without fiber diffusion, we show the statistics for filaments of length $L = 0.5$ μm (orange) and $L = 1$ μm (blue), where we observe dynamics occurring on a similar timescale, especially in the initial stage ($t \leq \tau_c \approx 20$) of bundling. (*b*) When we add fiber diffusion, the bundling process for $L = 0.5$ μm (purple) is significantly faster than $L = 1$ μm (yellow), because filaments can diffuse faster. Error bars are the error in the mean over five trials. To see this figure in color, go online.

CLs pull fibers together and align them, thereby allowing more CLs to bind to other sections of the fibers. What results initially, for times smaller than the critical bundling coalescence time τ_c, is a collection of bundles with a few highly aligned filaments, also called a composite bundle state (4). For times larger than τ_c, these bundles coalesce into larger bundles using a similar mechanism as that for individual fibers, and a clustered bundle state forms. Our critical bundling timescale τ_c thus describes the initial time at which networks transition from the composite bundle state to the clustered bundle state. In networks with fiber turnover, a clustered bundle steady state is only possible if the turnover time is much larger than τ_c (3). Although our work leaves unclear the role of steric interactions in slowing down bundling, we did show that the strong cross-linking present at later times is sufficient to arrest the bundling process. In fact, strong cross-linking provides a force somewhat equivalent to steric interactions, since the finite rest length of the CLs keeps linked filaments apart (see Note 23 in (46)). In this sense, our model properly treated the strong cross-linking limit, where the fibers are so constrained by the CLs that they do not overlap.

We quantified the role of diffusion throughout the bundling process, finding that it has a larger impact in the initial stages of bundling, when the filaments are not severely constrained by CLs and can move freely to find each other. We associated

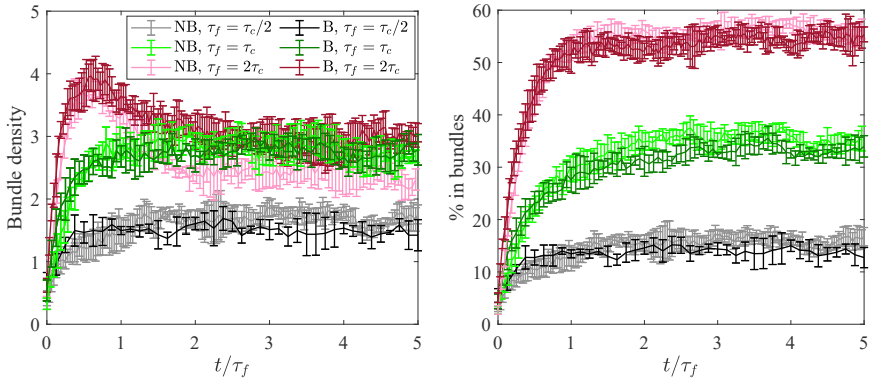

FIGURE 7 Steady-state morphologies for systems with turnover. We introduce filament turnover with mean filament lifetime τ_f (see (3) for implementation details) and observe the steady-state bundle density (left) and percentage of fibers in bundles (right) for $\tau_f/\tau_c = 1/2$ (black), 1 (green), and 2 (red). Note that using a constant τ_f/τ_c in the two systems ensures $\tau_f^{(B)}/\tau_f^{(NB)} = \tau_c^{(B)}/\tau_c^{(NB)}$. Using both non-Brownian (lighter colors, $\tau_c \approx 16$ s) and Brownian (darker colors, $\tau_c \approx 4$ s) filaments, we show that the steady-state bundling statistics are roughly the same when τ_f/τ_c is matched. Error bars are the error in the mean over five trials. To see this figure in color, go online.

this stage with $t<\tau_c$ and showed that adding thermal fluctuations decreases τ_c from 16 s to 4 s. We showed that the stage when bundles coalesce ($t>\tau_c$) is less affected by thermal diffusion (sped up by a factor of two), since at that stage, the filaments are constrained by CLs, which are more involved in bundle coalescence. This complements the observation in ((10 and 14)) that bundling occurs faster in a fluid-like environment, where filaments can move freely before kinetic arrest.

At first glance, the order of magnitude of τ_c that we obtained seems shorter than the characteristic bundling time obtained experimentally, which is generally reported to be on the order of minutes (29). The comparison is difficult, however, since experimental times generally include polymerization, and the bundling timescale in experiments is defined by the onset of the clustered bundle steady state, which is much later than the composite bundle state where we define τ_c. Nevertheless, the most instructive comparison is between our work and Fig. 4 in (10), which shows experimentally that the addition of 10% nucleates (which speeds up the polymerization process) gives a saturated bundled state after 100 s of polymerization and bundling, where the bundles are made of at least 15–30 filaments and are spaced some 10–20 μm apart. Given this observation, and the fact that bundling slows down over time, it is not difficult to imagine that the transition from the homogeneous state to the composite bundle state could take place on the order of 5–10 s after CLs are added to a system of (polymerized and capped) actin filaments.

Although diffusion of fibers speeds up the bundling process, we showed that it must be combined with a sufficient concentration of CLs for rapid bundling to occur. In particular, we showed that a high concentration of CLs (high CL binding rate) can induce bundling for filaments of any mesh size, with a critical bundling time τ_c that depends only weakly on the mesh size. By contrast, when the concentration of CLs is small, bundling is more difficult for any fixed mesh size and gets near impossible as the mesh size increases, as near-fiber contacts become less frequent. This is in accordance with a number of experimental papers (5,12) which find that bundling requires a critical CL concentration. In addition, because the fibers are in contact for a short time at larger mesh sizes, the system must be saturated with CLs for bundling to proceed at a reasonable rate. This saturation is less important at smaller mesh sizes, where fiber pairs come into contact more frequently. Translating our results to experimental parameters, we find that the ratio of the cross-linker concentration to the F-actin concentration that is needed for a particular bundling timescale decreases as the actin concentration increases, which is in accordance with existing experimental observations (see Fig. 3 in (5)).

As already mentioned, one of the drawbacks of some experimental studies is the sensitivity of the bundling time to the rate of actin polymerization. For example, it is shown in (10) (Fig. 4 *d*) that polymerization kinetics make an order of magnitude difference in the bundling kinetics. Although simultaneous polymerization and bundling also occurs in vivo, our study here allowed us to divorce bundling and polymerization by focusing on a fixed filament length. By doing this, we showed that shorter filaments bundle faster exclusively because they can diffuse faster, because without thermal fluctuations, we saw no difference in the bundling kinetics between short and long filaments. This clarifies why shorter actin filaments are able to associate more rapidly into bundles without the presence of a background actin mesh (12,14).

There are, of course, other timescales that we could have examined in the bundling process. For instance, Figs. S4 and S7 show that the timescale for slow down of the fibers' diffusivity, measured by the decay of their mean-square displacement, is related to but certainly not the same as the critical bundling time τ_c. Our choice to focus on the timescale τ_c was motivated by our observation in previous work (3) that the steady-state morphology of cross-linked actin networks is driven by a competition between bundling (which occurs on timescale τ_c) and filament turnover (which occurs on timescale τ_f). Although it is intuitively obvious that increasing the turnover timescale τ_f will produce a steady state with more bundles, it is fair to ask whether the ratio τ_f/τ_c alone controls the steady-state morphology or whether some other microscopic parameters come into play. In Fig. 7, we showed that, for turnover times $\tau_f = \tau_c/2$, τ_c, and $2\tau_c$, the gel evolves to a steady state, where the bundle density and percentage of fibers in bundles depend primarily on the ratio τ_f/τ_c for either Brownian or non-Brownian fibers (recall that τ_c differs by a factor of four for these two cases). Snapshots in Fig. S8 show little qualitative difference between the network morphology of the Brownian and non-Brownian steady states for a fixed τ_f/τ_c. Thus, for a fixed turnover time τ_f, the steady-state morphology is controlled by τ_c, which is the timescale we studied in detail here.

We can also extrapolate our results to the cell cytoskeleton, but this must be done with some caution because of the complexity of the in vivo system. The simulated actin network densities are characteristic of those observed in cell actin cortex, where mesh sizes are on the order 0.1 μm (45). Considering that the characteristic turnover times for the cell cortex are in the order of tens of seconds (47), longer than the characteristic bundling times our model predicts, the simple model prediction is that there is significant bundling in the cell cortex. However, to support this prediction, additional complexity, such as binding of filaments to the cell membrane and a mix of formin- and Arp2/3-generated filaments, will have to be added to the model. Similarly, in the future, the model could be modified to investigate effects of bundling rates that depend on mutual orientation of the filament pair (29).

Our study here used rigid filaments and coarse grained the dynamics of CL diffusion and binding. Although we showed that non-Brownian semiflexible actin filaments can be

approximated by rigid ones, we have not accounted for the transverse bending fluctuations in actin filaments. In some sense, softening the stiffness of the CLs, which gives a wider range of binding distances than might otherwise be possible, qualitatively accounts for this, but we plan to develop a numerical method that includes bending fluctuations in the future. We also hope to place our model of cross-linker dynamics on more rigorous footing by comparing it with a model that actually tracks the diffusion, binding, and unbinding of individual CLs. Other modeling studies addressed bundling in more complex systems, for example, formation of unipolar bundles from a branched actin network (48) and bundling in the presence of a mix of CLs and myosin molecular motors (35,49). Interestingly, the appearance of the bundles in these more complex systems (49), which form when CL concentration is above a threshold value (50), resemble those predicted by our model without motors. Another level of complexity is limits on bundle sizes due to chirality effects (51) and long-range electrostatic repulsion between the filaments (reviewed in (52)). Finally, in this work, it was too difficult for us to simulate the experimental steady-state, clustered, bundled morphologies, since we simulated actin filament lengths of 1 μm and the observed steady states have bundles separated by hundreds of microns (5,8). More efficient, graphics-processor-unit-based simulation techniques might enable the efficient simulation of even larger systems.

SUPPORTING MATERIAL

Supporting material can be found online at https://doi.org/10.1016/j.bpj.2022.02.030.

AUTHOR CONTRIBUTIONS

O.M., A.D., and A.M. designed the research. O.M. carried out all simulations and analyzed the data. O.M., A.D., and A.M. wrote the article.

ACKNOWLEDGMENTS

This work was supported by the National Science Foundation through Research Training Group in Modeling and Simulation under award RTG/DMS-1646339 and through the Division of Mathematical Sciences award DMS-2052515. O.M. is supported by the National Science Foundation via GRFP/DGE-1342536, and A.M. is supported by National Science Foundation grant DMS-1953430. Code and input files for the simulations are available at https://github.com/stochasticHydroTools/SlenderBody. All of our simulations were run on the New York University High Performance Computing Greene Supercomputer cluster.

REFERENCES

1. Alberts, B., A. Johnson, …, P. Walter. 2002. Molecular Biology of the Cell. Garland Science.
2. Chaubet, L., A. R. Chaudhary, …, A. G. Hendricks. 2020. Dynamic actin cross-linking governs the cytoplasm's transition to fluid-like behavior. *Mol. Biol. Cell.* 31:1744–1752.
3. Maxian, O., R. P. Peláez, …, A. Donev. 2021. Simulations of dynamically cross-linked actin networks: morphology, rheology, and hydrodynamic interactions. *PLoS Comput. Biol.* 17:e1009240.
4. Lieleg, O., M. M. Claessens, and A. R. Bausch. 2010. Structure and dynamics of cross-linked actin networks. *Soft Matter.* 6:218–225.
5. Schmoller, K., O. Lieleg, and A. Bausch. 2009. Structural and viscoelastic properties of actin/filamin networks: cross-linked versus bundled networks. *Biophys. J.* 97:83–89.
6. Hou, L., K. Luby-Phelps, and F. Lanni. 1990. Brownian motion of inert tracer macromolecules in polymerized and spontaneously bundled mixtures of actin and filamin. *J. Cell Biol.* 110:1645–1654.
7. Gardel, M., J. H. Shin, …, D. Weitz. 2004. Elastic behavior of cross-linked and bundled actin networks. *Science.* 304:1301–1305.
8. Lieleg, O., K. M. Schmoller, …, A. R. Bausch. 2009. Structural polymorphism in heterogeneous cytoskeletal networks. *Soft Matter.* 5:1796–1803.
9. Wachsstock, D. H., W. Schwartz, and T. D. Pollard. 1993. Affinity of alpha-actinin for actin determines the structure and mechanical properties of actin filament gels. *Biophys. J.* 65:205.
10. Falzone, T. T., M. Lenz, …, M. L. Gardel. 2012. Assembly kinetics determine the architecture of α-actinin crosslinked F-actin networks. *Nat. Commun.* 3:1–9.
11. Foffano, G., N. Levernier, and M. Lenz. 2016. The dynamics of filament assembly define cytoskeletal network morphology. *Nat. Commun.* 7:1–8.
12. Kasza, K., C. Broedersz, …, D. Weitz. 2010. Actin filament length tunes elasticity of flexibly cross-linked actin networks. *Biophys. J.* 99:1091–1100.
13. Ma, R., and J. Berro. 2018. Structural organization and energy storage in crosslinked actin assemblies. *PLoS Comput. Biol.* 14:e1006150.
14. Weirich, K. L., S. Banerjee, …, M. L. Gardel. 2017. Liquid behavior of cross-linked actin bundles. *P. Natl. Acad. Sci. U S A.* 114:2131–2136.
15. Tempel, M., G. Isenberg, and E. Sackmann. 1996. Temperature-induced sol-gel transition and microgel formation in α-actinin cross-linked actin networks: a rheological study. *Phys. Rev. E.* 54:1802.
16. Borukhov, I., R. F. Bruinsma, …, A. J. Liu. 2005. Structural polymorphism of the cytoskeleton: a model of linker-assisted filament aggregation. *P. Natl. Acad. Sci. U S A.* 102:3673–3678.
17. Zilman, A., and S. Safran. 2003. Role of cross-links in bundle formation, phase separation and gelation of long filaments. *Europhys. Lett.* 63:139.
18. Kierfeld, J., T. Kühne, and R. Lipowsky. 2005. Discontinuous unbinding transitions of filament bundles. *Phys. Rev. Lett.* 95:038102.
19. Yu, X., and A. Carlsson. 2004. Kinetics of filament bundling with attractive interactions. *Biophys. J.* 87:3679–3689.
20. Kim, T., W. Hwang, and R. Kamm. 2009. Computational analysis of a cross-linked actin-like network. *Exp. Mech.* 49:91–104.
21. Maxian, O., A. Mogilner, and A. Donev. 2021. Integral-based spectral method for inextensible slender fibers in Stokes flow. *Phys. Rev. Fluids.* 6:014102.
22. Gittes, F., B. Mickey, …, J. Howard. 1993. Flexural rigidity of microtubules and actin filaments measured from thermal fluctuations in shape. *J. Cell Biol.* 120:923–934.
23. Tornberg, A.-K., and M. J. Shelley. 2004. Simulating the dynamics and interactions of flexible fibers in Stokes flows. *J. Comput. Phys.* 196:8–40.
24. Keller, J. B., and S. I. Rubinow. 1976. Slender-body theory for slow viscous flow. *J. Fluid Mech.* 75:705–714.
25. Johnson, R. E. 1980. An improved slender-body theory for Stokes flow. *J. Fluid Mech.* 99:411–431.
26. Courson, D. S., and R. S. Rock. 2010. Actin cross-link assembly and disassembly mechanics for α-actinin and fascin. *J. Biol. Chem.* 285:26350–26357.
27. Gillespie, D. T. 2007. Stochastic simulation of chemical kinetics. *Annu. Rev. Phys. Chem.* 58:35–55.

28. Anderson, D. F. 2007. A modified next reaction method for simulating chemical systems with time dependent propensities and delays. *J. Chem. Phys.* 127:214107.
29. Meyer, R. K., and U. Aebi. 1990. Bundling of actin filaments by alpha-actinin depends on its molecular length. *J. Cell Biol.* 110:2013–2024.
30. Sprinkle, B., F. Balboa Usabiaga, …, A. Donev. 2017. Large scale Brownian dynamics of confined suspensions of rigid particles. *J. Chem. Phys.* 147:244103.
31. Westwood, T. A., B. Delmotte, and E. E. Keaveny. 2021. A generalised drift-correcting time integration scheme for Brownian suspensions of rigid particles with arbitrary shape. Preprint at arXiv:2106.00449.
32. Zero, K., and R. Pecora. 1982. Rotational and translational diffusion in semidilute solutions of rigid-rod macromolecules. *Macromolecules.* 15:87–93.
33. Makino, M., and M. Doi. 2004. Brownian motion of a particle of general shape in Newtonian fluid. *J. Phys. Soc. Jpn.* 73:2739–2745.
34. Delong, S., F. Balboa Usabiaga, and A. Donev. 2015. Brownian dynamics of confined rigid bodies. *J. Chem. Phys.* 143:144107.
35. Bidone, T. C., W. Jung, …, T. Kim. 2017. Morphological transformation and force generation of active cytoskeletal networks. *PLoS Comput. Biol.* 13:e1005277.
36. Evans, D. J., D. J. Searles, and S. R. Williams. 2016. Fundamentals of Classical Statistical Thermodynamics: Dissipation, Relaxation, and Fluctuation Theorems. John Wiley & Sons.
37. Morse, D. C. 1998. Viscoelasticity of concentrated isotropic solutions of semiflexible polymers. 1. model and stress tensor. *Macromolecules.* 31:7030–7043.
38. Grazi, E. 1997. What is the diameter of the actin filament? *FEBS Lett.* 405:249–252.
39. Janmey, P. A., S. Hvidt, …, T. P. Stossel. 1994. The mechanical properties of actin gels. Elastic modulus and filament motions. *J. Biol. Chem.* 269:32503–32513.
40. McGrath, J. L., E. A. Osborn, …, J. H. Hartwig. 2000. Regulation of the actin cycle *in vivo* by actin filament severing. *P. Natl. Acad. Sci. USA.* 97:6532–6537.
41. Luby-Phelps, K. 1999. Cytoarchitecture and physical properties of cytoplasm: volume, viscosity, diffusion, intracellular surface area. *In* International Review of Cytology. Elsevier, pp. 189–221.
42. Le, S., X. Hu, …, J. Yan. 2017. Mechanotransmission and mechanosensing of human alpha-actinin 1. *Cell Rep.* 21:2714–2723.
43. Kuhlman, P. A., J. Ellis, …, C. R. Bagshaw. 1994. The kinetics of the interaction between the actin-binding domain of α-actinin and F-actin. *FEBS Lett.* 339:297–301.
44. Xu, J., D. Wirtz, and T. D. Pollard. 1998. Dynamic cross-linking by α-actinin determines the mechanical properties of actin filament networks. *J. Biol. Chem.* 273:9570–9576.
45. Eghiaian, F., A. Rigato, and S. Scheuring. 2015. Structural, mechanical, and dynamical variability of the actin cortex in living cells. *Biophys. J.* 108:1330–1340.
46. Müller, K. W., R. F. Bruinsma, …, A. J. Levine. 2014. Rheology of semiflexible bundle networks with transient linkers. *Phys. Rev. Lett.* 112:238102.
47. Fritzsche, M., A. Lewalle, …, G. Charras. 2013. Analysis of turnover dynamics of the submembranous actin cortex. *Mol. Biol. Cell.* 24:757–767.
48. Yang, L., D. Sept, and A. Carlsson. 2006. Energetics and dynamics of constrained actin filament bundling. *Biophys. J.* 90:4295–4304.
49. Popov, K., J. Komianos, and G. A. Papoian. 2016. MEDYAN: mechanochemical simulations of contraction and polarity alignment in actomyosin networks. *PLoS Comput. Biol.* 12:e1004877.
50. Chandrasekaran, A., A. Upadhyaya, and G. A. Papoian. 2019. Remarkable structural transformations of actin bundles are driven by their initial polarity, motor activity, crosslinking, and filament treadmilling. *PLoS Comput. Biol.* 15:e1007156.
51. Grason, G. M. 2015. Colloquium: geometry and optimal packing of twisted columns and filaments. *Rev. Mod. Phys.* 87:401.
52. Schnauß, J., T. Händler, and J. A. Käs. 2016. Semiflexible biopolymers in bundled arrangements. *Polymers.* 8:274.

Biophysical Journal, Volume *121*

Supplemental information

Interplay between Brownian motion and cross-linking controls bundling dynamics in actin networks

Ondrej Maxian, Aleksandar Donev, and Alex Mogilner

Supplemental text

Interplay between Brownian motion and cross-linking kinetics controls bundling dynamics in actin networks

Ondrej Maxian, Aleksandar Donev, and Alex Mogilner

A Rigid fibers as a special case of inextensible fibers

In [S1], we discretized the inextensible system Eq. (2) (equation numbers refer to the article main text) by discretizing each fiber with N Chebyshev collocation points and representing the functions $\alpha_1(s)$ and $\alpha_2(s)$ by their Chebyshev coefficients, $\alpha_j(s) = \sum_{k=0}^{N-2} \alpha_{jk} T_k(s)$. Our goal here is to show that setting $\alpha_j(s) = \alpha_j = \text{const.}$ instead gives the straight rigid fiber kinematic operators Eqs. (8) and (9). For convenience, we first restate the kinematic equations for inextensible fibers, which are Equations (41) and (44) in [S1],

$$(\boldsymbol{\mathcal{K}}[\boldsymbol{X}]\boldsymbol{\alpha})(s) = \overline{\boldsymbol{U}} + \int_0^s \sum_{j=1}^{2} \sum_k \alpha_{jk} T_k\left(s'\right) \boldsymbol{n}_j\left(\boldsymbol{\tau}(s')\right)\, ds' \tag{S1}$$

$$\boldsymbol{\mathcal{K}}^*[\boldsymbol{X}]\boldsymbol{\lambda} := \begin{pmatrix} \int_0^L \left(\int_0^s T_k(s') \boldsymbol{n}_1\left(\boldsymbol{\tau}(s')\right)\, ds'\right) \cdot \boldsymbol{\lambda}(s)\, ds \\ \int_0^L \left(\int_0^s T_k(s') \boldsymbol{n}_2\left(\boldsymbol{\tau}(s')\right)\, ds'\right) \cdot \boldsymbol{\lambda}(s)\, ds \\ \int_0^L \boldsymbol{\lambda}(s)\, ds \end{pmatrix} = \begin{pmatrix} 0 \\ 0 \\ \boldsymbol{0} \end{pmatrix}, \tag{S2}$$

where the first two components of (S2) hold for all k. Let us denote by $\boldsymbol{\mathcal{K}}_s$ the operator $\boldsymbol{\mathcal{K}}$ in the case of straight fibers with $k = 0$ being the only included Chebyshev mode, and likewise for $\boldsymbol{\mathcal{K}}^*$. Then, since the fibers are straight, the orthonormal frame $(\boldsymbol{\tau}, \boldsymbol{n}_1, \boldsymbol{n}_2)$ is constant along the fiber, and thus $\boldsymbol{\mathcal{K}}_s$ and $\boldsymbol{\mathcal{K}}_s^*$ simplify to

$$\boldsymbol{\mathcal{K}}_s\boldsymbol{\alpha} = \overline{\boldsymbol{U}} + \alpha_1 \boldsymbol{n}_1 s + \alpha_2 \boldsymbol{n}_2 s \tag{S3}$$

$$\boldsymbol{\mathcal{K}}_s^*\boldsymbol{\lambda} = \begin{pmatrix} \boldsymbol{n}_1 \cdot \int_0^L s\boldsymbol{\lambda}(s)\, ds \\ \boldsymbol{n}_2 \cdot \int_0^L s\boldsymbol{\lambda}(s)\, ds \\ \int_0^L \boldsymbol{\lambda}(s)\, ds \end{pmatrix}. \tag{S4}$$

We now want to show that $\boldsymbol{\mathcal{K}}_s$ and $\boldsymbol{\mathcal{K}}_r$ (defined in Eq. (8)) parameterize the same linear space of rigid motions. To do this, let us write $\boldsymbol{X}$ in Eq. (8) as an integral of the tangent vector

$$\begin{aligned}
\boldsymbol{\mathcal{K}}_r\boldsymbol{\alpha} &= \boldsymbol{U}_c + \boldsymbol{\Omega}\times(\boldsymbol{X}_0 + s\boldsymbol{\tau} - \boldsymbol{X}_c) && \text{(S5)}\\
&= \boldsymbol{U}_c + \boldsymbol{\Omega}\times(\boldsymbol{X}_0 - \boldsymbol{X}_c) + s\boldsymbol{\Omega}\times\boldsymbol{\tau} && \text{(S6)}\\
&= \widehat{\boldsymbol{U}}_c + s\left((\boldsymbol{\Omega}\cdot\boldsymbol{\tau})\,\boldsymbol{\tau} + (\boldsymbol{\Omega}\cdot\boldsymbol{n}_1)\,\boldsymbol{n}_1 + (\boldsymbol{\Omega}\cdot\boldsymbol{n}_2)\,\boldsymbol{n}_2\right)\times\boldsymbol{\tau} && \text{(S7)}\\
&= \widehat{\boldsymbol{U}}_c + s\left(-(\boldsymbol{\Omega}\cdot\boldsymbol{n}_1)\,\boldsymbol{n}_2 + (\boldsymbol{\Omega}\cdot\boldsymbol{n}_2)\,\boldsymbol{n}_1\right). && \text{(S8)}
\end{aligned}$$

This is exactly the form of $\boldsymbol{\mathcal{K}}_s$ in (S3) with $\alpha_1 = -\boldsymbol{\Omega}\cdot\boldsymbol{n}_2$ and $\alpha_2 = -\boldsymbol{\Omega}\cdot\boldsymbol{n}_1$. So $\boldsymbol{\mathcal{K}}_r$ and $\boldsymbol{\mathcal{K}}_s$ parameterize the same space.

To complete the equivalence, we now show that $\boldsymbol{\mathcal{K}}_s^*\boldsymbol{\lambda} = \boldsymbol{0}$ iff $\boldsymbol{\mathcal{K}}_r^*\boldsymbol{\lambda} = \boldsymbol{0}$. Obviously, $\int_0^L \boldsymbol{\lambda}(s)\,ds = \boldsymbol{0}$ in both cases, so we only have to deal with the torque constraint. If we use the fact that $\int_0^L \boldsymbol{\lambda}(s)\,ds = \boldsymbol{0}$, we can write the second component of Eq. (9) as

$$\begin{aligned}
\boldsymbol{\mathcal{K}}_r^*\boldsymbol{\lambda} &= \int_0^L (\boldsymbol{X}(s) - \boldsymbol{X}_c)\times\boldsymbol{\lambda}(s)\,ds = \int_0^L \boldsymbol{X}(s)\times\boldsymbol{\lambda}(s)\,ds = \int_0^L s\boldsymbol{\tau}\times\boldsymbol{\lambda}(s)\,ds && \text{(S9)}\\
&= \int_0^L s\boldsymbol{\tau}\times\left((\boldsymbol{\tau}\cdot\boldsymbol{\lambda}(s))\,\boldsymbol{\tau} + (\boldsymbol{n}_1\cdot\boldsymbol{\lambda}(s))\,\boldsymbol{n}_1 + (\boldsymbol{n}_2\cdot\boldsymbol{\lambda}(s))\,\boldsymbol{n}_2\right)\,ds && \text{(S10)}\\
&= -\boldsymbol{n}_1\left(\boldsymbol{n}_2\cdot\int_0^L s\boldsymbol{\lambda}(s)\,ds\right) + \boldsymbol{n}_2\left(\boldsymbol{n}_1\cdot\int_0^L s\boldsymbol{\lambda}(s)\,ds\right) && \text{(S11)}
\end{aligned}$$

And now, since $\boldsymbol{n}_1$ and $\boldsymbol{n}_2$ are orthogonal and nonzero, we see from (S4) that $\boldsymbol{\mathcal{K}}_s^*\boldsymbol{\lambda} = \boldsymbol{0} \leftrightarrow \boldsymbol{\mathcal{K}}_r^*\boldsymbol{\lambda} = \boldsymbol{0}$. This shows that we can implement rigid fibers using the same algorithms as in [S1], except we just need to keep a single ($k = 0$) Chebyshev polynomial. Note that the value of κ we use does not matter except for numerical stability since the fibers stay straight for all time, and so we set $\kappa = 0$.

B Form and coefficients of the rigid body mobility matrix

Because of the symmetry of the fiber, the mobility matrix and its "square root" for a single fiber can be written in the form

$$\begin{aligned}
\boldsymbol{N}_{\mathrm{tt}} &= \frac{1}{\mu L}\left(\alpha(\epsilon)\boldsymbol{I} + \beta(\epsilon)\boldsymbol{\tau}\boldsymbol{\tau}\right), \qquad \boldsymbol{N}_{\mathrm{tt}}^{1/2} = \frac{1}{\sqrt{\mu L}}\left(\sqrt{\alpha}\boldsymbol{I} + \left(-\sqrt{\alpha} + \sqrt{\alpha+\beta}\right)\boldsymbol{\tau}\boldsymbol{\tau}\right), && \text{(S12)}\\
\boldsymbol{N}_{\mathrm{rr}} &= \frac{\gamma(\epsilon)}{\mu L^3}\left(\boldsymbol{I} - \boldsymbol{\tau}\boldsymbol{\tau}\right), \qquad \boldsymbol{N}_{\mathrm{rr}}^{1/2} = \sqrt{\frac{\gamma}{\mu L^3}}\left(\boldsymbol{I} - \boldsymbol{\tau}\boldsymbol{\tau}\right).
\end{aligned}$$

Notice that the rotational mobility has a null space of the tangent vector $\boldsymbol{\tau}$. The dimensionless coefficients α, β, and γ are given for various ϵ in Table S1.

ϵ	$\alpha^{(\mathrm{FP})}$	$\beta^{(\mathrm{FP})}$	$\gamma^{(\mathrm{FP})}$
0.01	0.3841	0.2230	3.4263
0.008	0.4020	0.2413	3.6412
0.006	0.4251	0.2646	3.9179
0.005	0.4396	0.2793	4.0931
0.004	0.4575	0.2973	4.3073
0.002	0.5129	0.3530	4.9721
0.001	0.5682	0.4085	5.6361

Table S1: Mobility coefficients for the 6×6 rigid body mobility matrix $\boldsymbol{N}$ defined in (S12) for straight fibers. The numerical estimate of the matrix $\boldsymbol{N}$ is related to the slender body mobility $\boldsymbol{M}$ in Eq. (11), which is computed using intra-fiber hydrodynamics as discussed in the main text section on the mobility.

C Temporal integrator for fluctuating fibers

In this section, we show that our temporal integrator for Brownian motion can accurately reproduce the steady state distribution of link strains. We place two parallel fibers a distance 0.05 apart, so that initially $\boldsymbol{X}^{(1)}(s) = (s, 0, 0)$ and $\boldsymbol{X}^{(2)}(s) = (s, 0.05, 0)$. At $t = 0$, the fibers are connected by a permanent CL attached at the point $s = L = 1$ on each fiber. We use rigid fibers with $N = 50$ points, CL variance $\sigma/L = 0.005$ (to simulate point-force-like springs), spring stiffness $K_c = 10$ pN/μm, and rest length $\ell = 0.05$ μm. We use $\epsilon = 0.004$, $\mu = 0.1$ Pa·s, and $L = 1$ μm, as we do in most of the simulations in the main text. Because we are not interested in dynamics here, we use the local drag mobility, which is Eq. (4) without the integral term. The maximum stable time step is $\Delta t = 0.005$ s, and so we will simulate both with $\Delta t = 0.0005$ s (to get results with small temporal error) and $\Delta t = 0.0025$ s (which is close to the stability limit). We simulate until $t = 100$ seconds in both cases and verify that we run for long enough that we have reached the steady state.

We expect the steady state probability density function (pdf) to be the Gibbs-Boltzmann distribution

$$P(x) = Zx^2 \exp\left(-\frac{K_c(x-\ell)^2}{2kT}\right), \tag{S13}$$

where the constant Z is chosen such that $\int_0^\infty P(x)\,dx = 1$, and the Jacobian x^2 factor is necessary because $P(x)$ is actually the one-dimensional analogue of the true three-dimensional distribution $P(\|\boldsymbol{x}\|)$. Figure S1 (left) shows that the steady state distribution with small Δt agrees with the theory (S13). The right plot, which gives the distributions for Δt =50% of the stability limit, shows

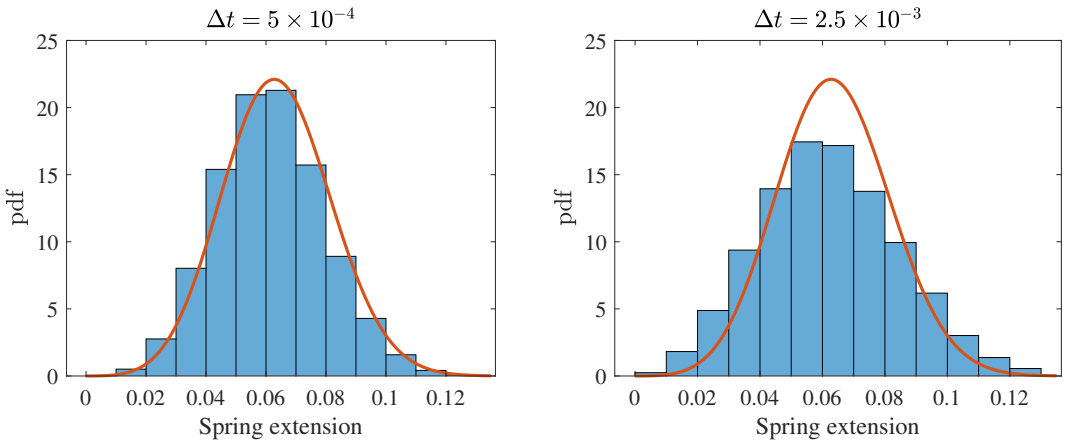

Figure S1: Steady state spring length distribution for two stiff fibers connected by a spring at their endpoint with rest length $\ell = 0.05$ μm. Histograms are the data, and red lines are (S13). Here we use rigid fibers with $N = 50$ points, CL variance $\sigma/L = 0.005$, and spring stiffness $K_c = 10$ pN/μm. We show $\Delta t = 5 \times 10^{-4}$ s =10% of the stability limit on the left, and $\Delta t = 2.5 \times 10^{-3}$ s =50% of the stability limit on the right. The spring extension measurement is performed at the midpoint of the time step (after step 1 in the Temporal Integration section of the main text).

that our temporal integrator can still reproduce the correct distribution with a larger time step size.

References

[S1] Ondrej Maxian, Alex Mogilner, and Aleksandar Donev. Integral-based spectral method for inextensible slender fibers in stokes flow. *Physical Review Fluids*, 6(1):014102, 2021.

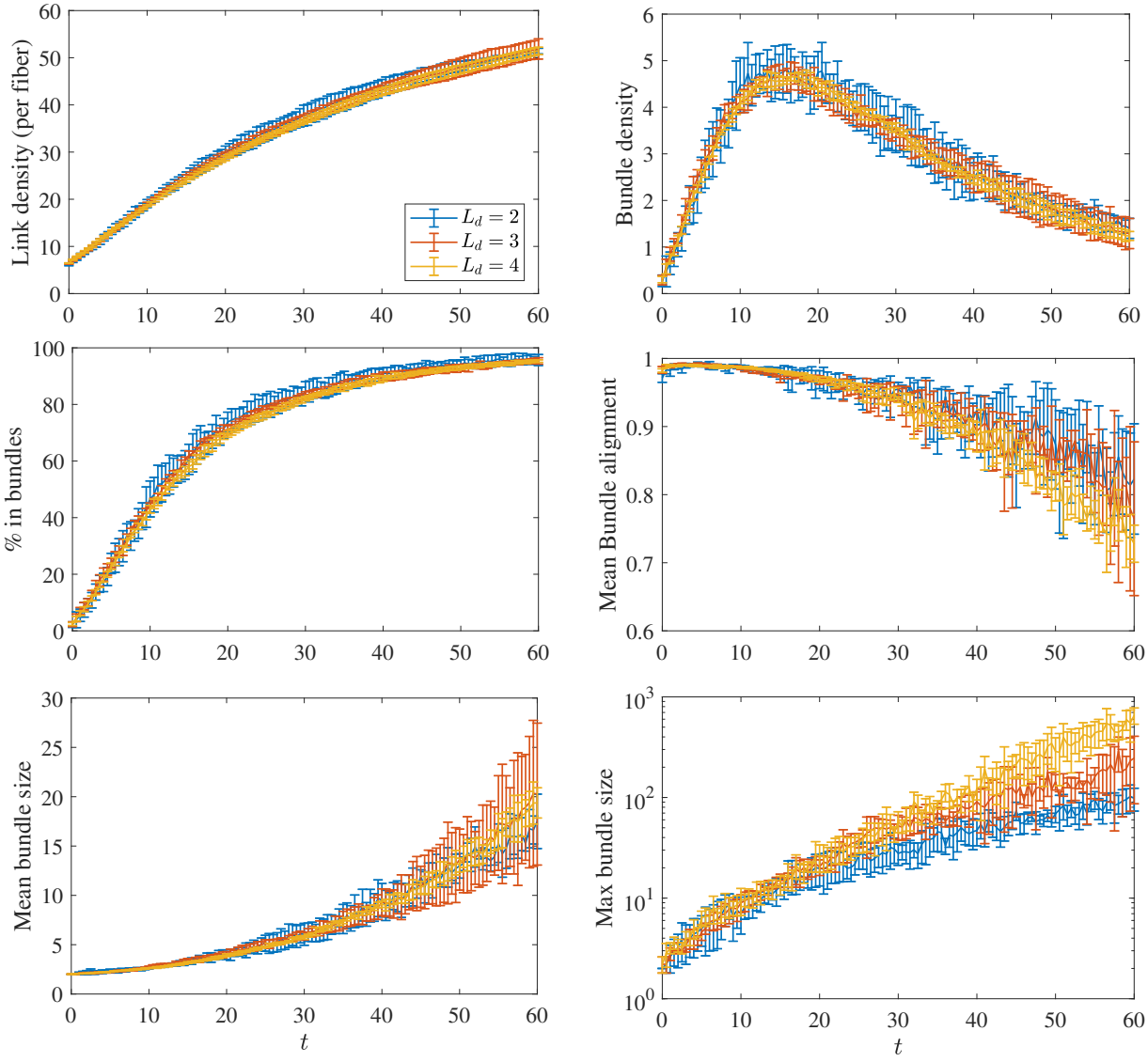

Figure S2: Link density, bundle density, % of fibers in bundles, mean bundle alignment, mean bundle size, and maximum bundle size, in a network of semiflexible ($\kappa = 0.07$ pN·μm^2) non-Brownian filaments with initial mesh size $\ell_m = 0.2$ μm. We show curves with different domain sizes (in μm) to establish that the statistics are repeatable in larger systems. The only statistic which is not repeatable is the maximum bundle size after many of the filaments have collapsed into one bundle ($t \gtrsim 40$ s).

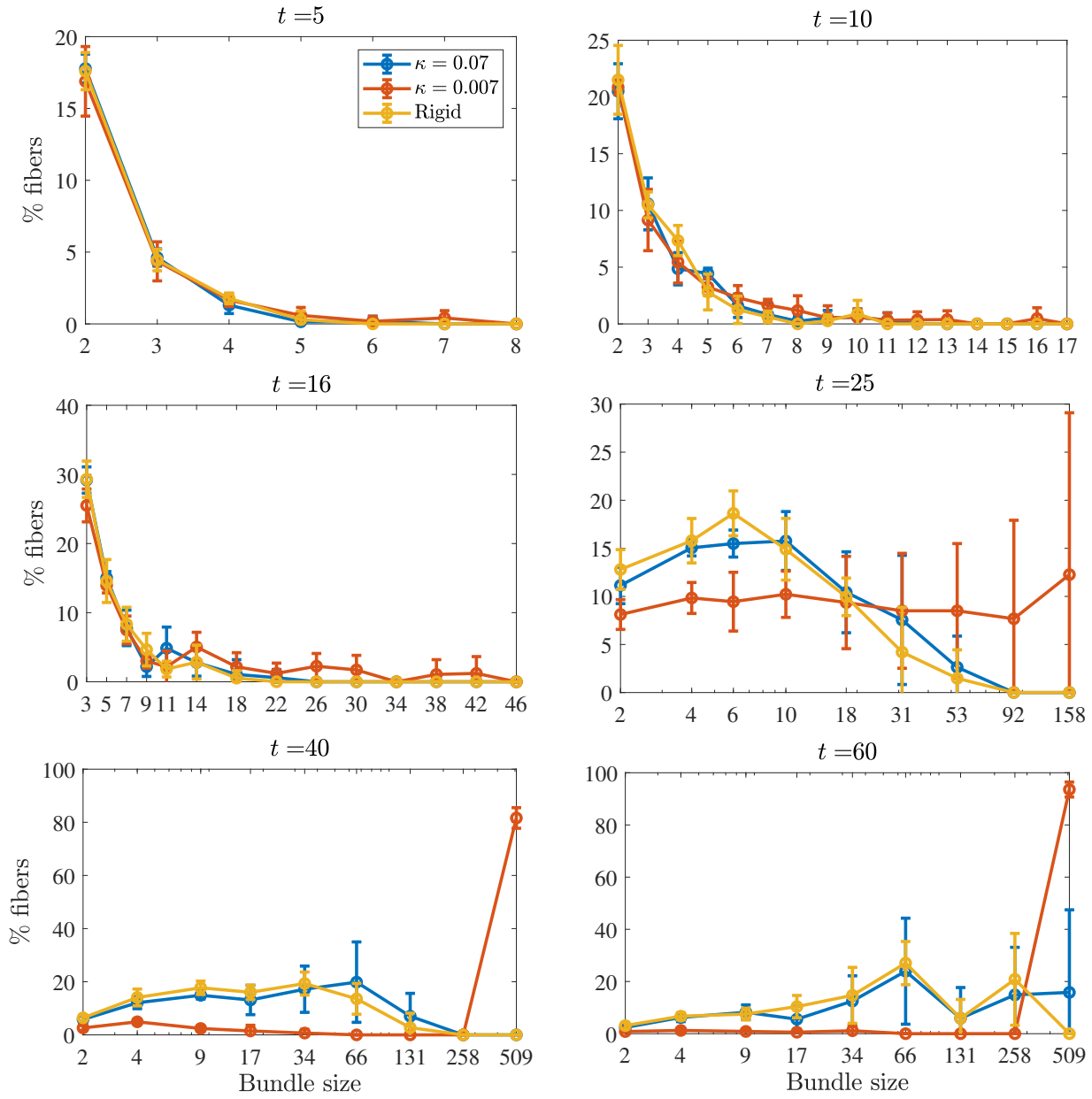

Figure S3: Bundle sizes over time in the system with $F = 675$ semiflexible filaments in a domain of size $L_d = 3$ μm ($\tau_c \approx 16$). We show the percentage of fibers that are in bundles of various sizes over time for $\kappa = 0.07$ pN$\cdot\,\mu$m^2 (blue), $\kappa = 0.007$ pN$\cdot\,\mu$m^2 (orange), and rigid fibers (yellow). For times $t = 25, 40$, and 60 seconds, the x coordinate reflects the center of a histogram bin with logarithmically-scaled width. At $t = 5$ s, 25% of the filaments are in bundles of sizes 2 or 3, while most of the other fibers are not in bundles. At $t = \tau_c = 16$ s, about 50% of the fibers are in bundles of size 10 or less, with a small percentage in larger bundles, and the rest not in bundles at all (this is the composite bundle state). For semiflexible fibers with $\kappa = 0.07$ and rigid fibers, about 75% of the fibers are in bundles of size 30 or larger by $t = 60$, while for fibers with $\kappa = 0.007$ the entire suspension has coalesced together by $t = 40$ seconds.

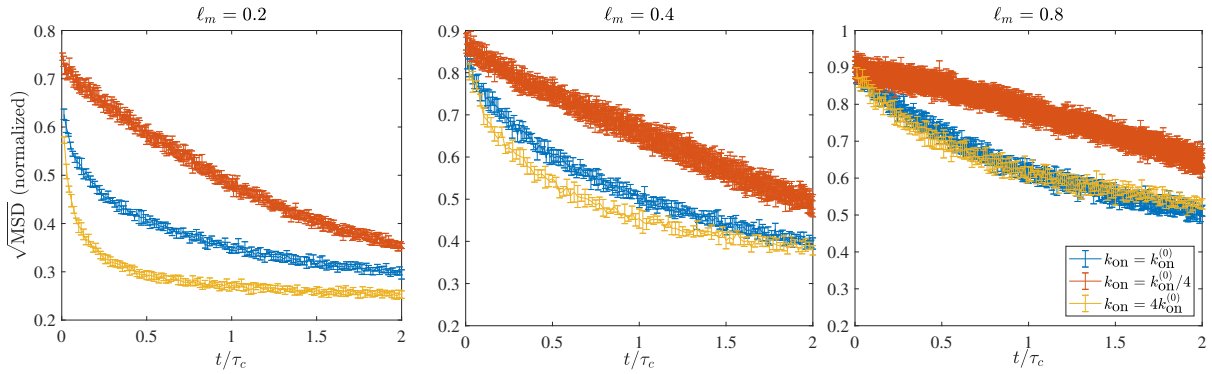

Figure S4: Square root of average mean square displacement of the fibers' centers over a time span of 0.05 seconds for simulations with Brownian dynamics and varying k_{on} (colors) and mesh size (from small mesh size to large going from left to right), all normalized by the value for a freely diffusing fiber. We normalize time by τ_c. While all of the curves show significant decay on the timescale τ_c, it is clear that τ_c is not the only timescale in the problem, since curves with small k_{on} are qualitatively different. This is not a surprise, since we saw in the main text that the bundling process with small k_{on} is more biased towards large bundles (see Fig. 5).

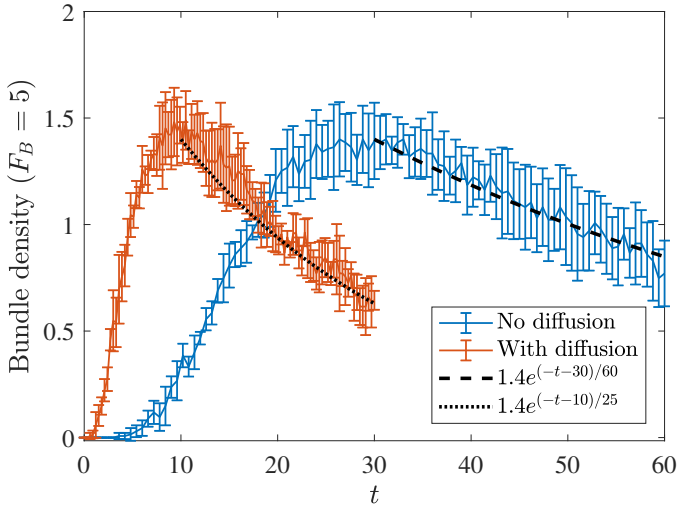

Figure S5: Comparing Brownian and non-Brownian filaments with a minimum of $F_B = 5$ filaments per bundle. In Fig. 3 in the main text, we used a definition of a bundle as having at least two filaments to conclude that Brownian motion accelerates the bundling process by more in the initial stages (factor of about 4) than in the latter (factor of about 2). When we increase to $F_B = 5$ filaments per bundle, we observe the same characteristic growth and decay as with $F_B = 2$, with the peak occurring three-fold faster in simulations with Brownian dynamics and the later dynamics being accelerated by a factor of about two (from a timescale of 60 s to 25 s). These confirm the qualitative (and quantitative) conclusions from Fig. 3 that we made in the main text.

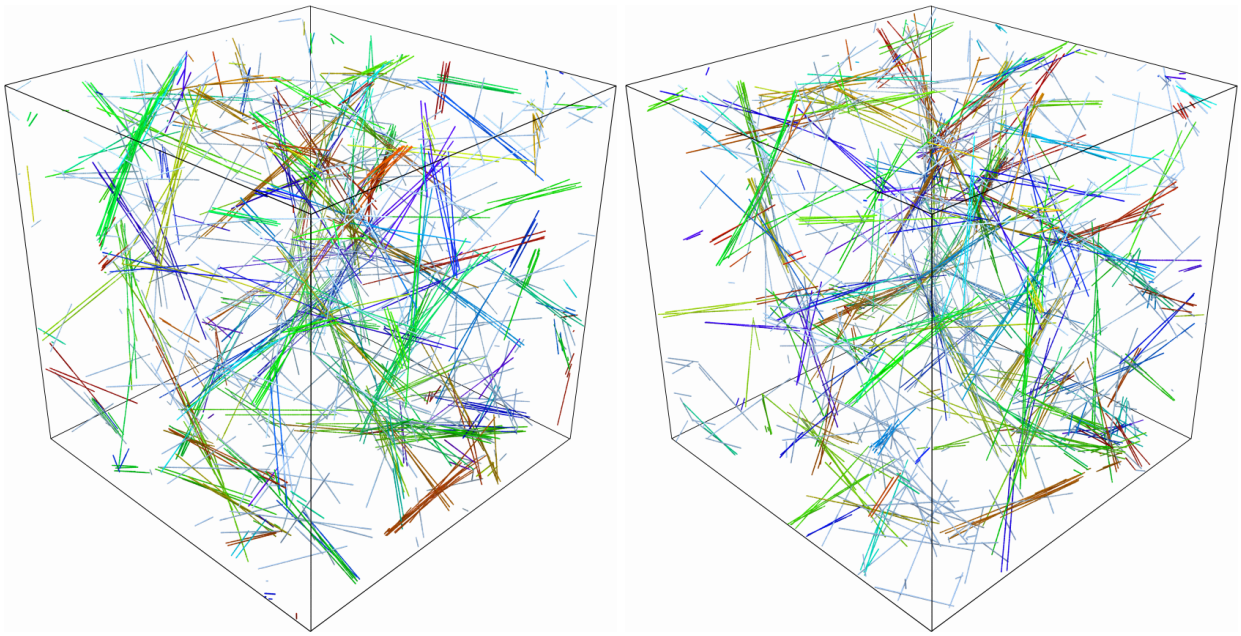

Figure S6: Representative snapshots of a network of rigid fibers without (left) and with (right) Brownian motion. Both snapshots are taken at $t = \tau_c$, which is 16 seconds for simulations without fluctuations and 4 seconds for simulations with fluctuations. The networks are qualitatively the same.

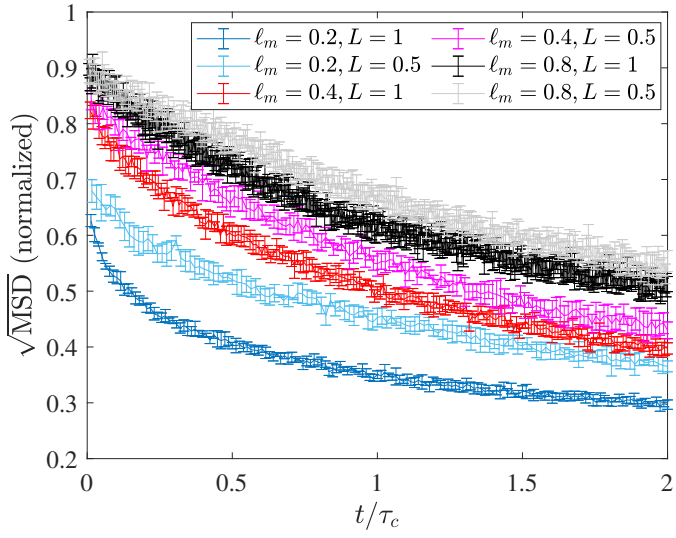

Figure S7: Decay of fibers' centers' displacement for different fiber lengths and mesh sizes. We show (the square root of) the average MSD of the fibers' centers over a time span of 0.05 seconds, normalized by the free space diffusion for fibers of the same length. We show mesh size $\ell_m = 0.2$ μm (blue), 0.4 μm (red), and 0.8 μm (black). Lighter colors are for filament length $L = 0.5$ μm, darker are $L = 1$ μm.

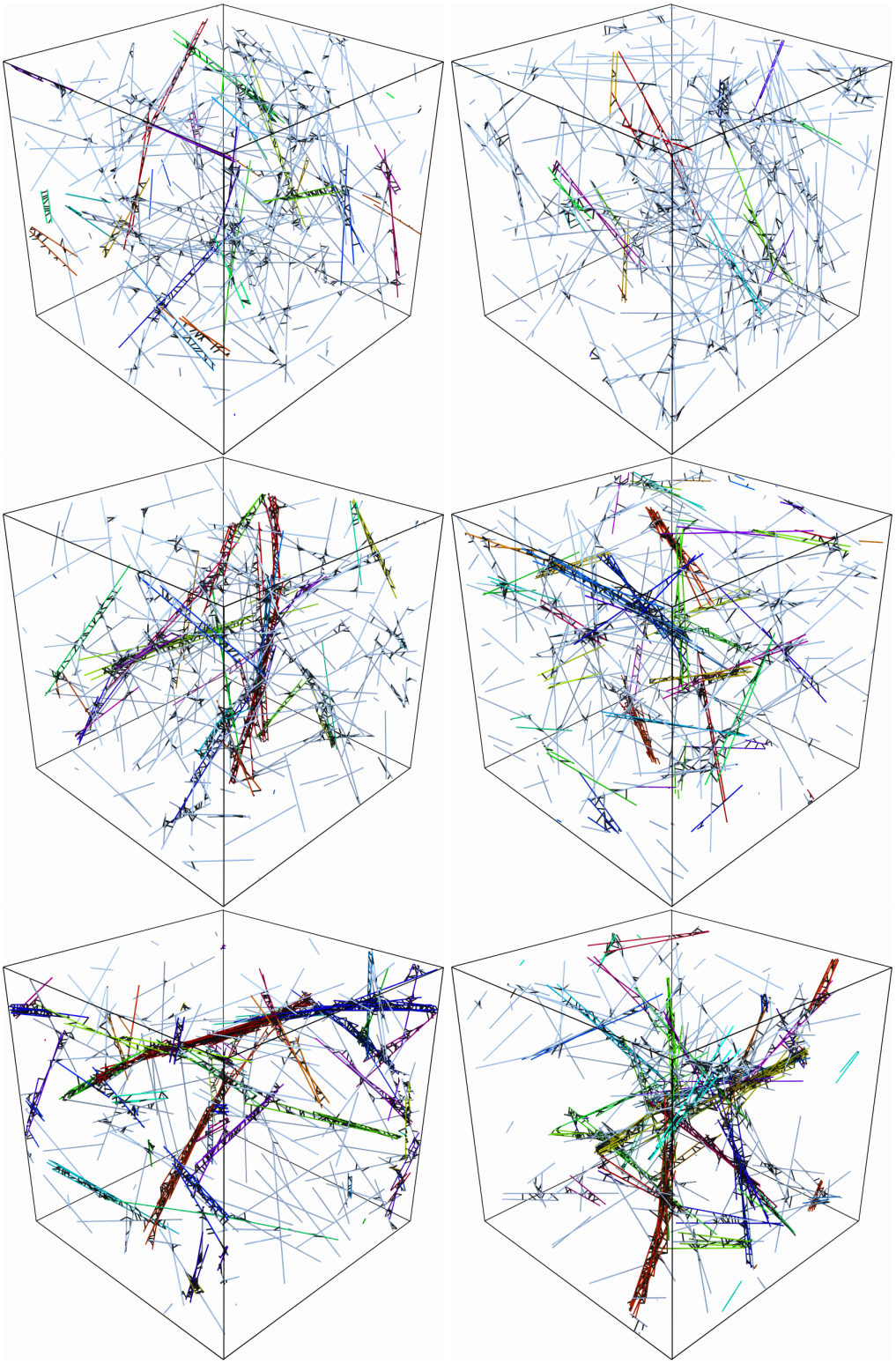

Figure S8: Steady states with fiber turnover for (top to bottom) $\tau_f = \tau_c/2$, $\tau_f = \tau_c$, and $\tau_f = 2\tau_c$ for a system with $L_d = 2$ and $\ell_m = 0.2$. The left column is for non-Brownian fibers ($\tau_c = 16$ seconds) and the right column is for Brownian ones ($\tau_c = 4$ seconds). There is little qualitative difference between the left and right columns, which indicates that the network morphology is controlled primarily by the ratio τ_f/τ_c.